Article:
Kauffmann, G., Millán-Irigoyen, I., Crowther, P. et al. (1 more author) (2024) A resolved study of the inner regions of nearby galaxies with an excess of young massive stars: missing link in the AGN–starburst connection? Monthly Notices of the Royal Astronomical Society, 527 (1). pp. 150-170. ISSN 0035-8711

https://doi.org/10.1093/mnras/stad3096

Monthly Notices of the ROYAL ASTRONOMICAL SOCIETY

MNRAS **527,** 150–170 (2024) https://doi.org/10.1093/mnras/stad3096
Advance Access publication 2023 October 12

A resolved study of the inner regions of nearby galaxies with an excess of young massive stars: missing link in the AGN–starburst connection?

Guinevere Kauffmann,[1]★ Iker Millán-Irigoyen,[2] Paul Crowther[3] and Claudia Maraston[4]

[1]*Max-Planck Institut für Astrophysik, D-85741 Garching, Germany*
[2]*Departamento de Investigacion Basica, CIEMAT, Avenida Complutense 40, E-28040, Madrid, Spain*
[3]*Department of Physics and Astronomy, University of Sheffield, Sheffield S3 7RH, UK*
[4]*Institute of Cosmology, University of Portsmouth, Burnaby Road, Portsmouth PO1 3FX, UK*

Accepted 2023 October 6. Received 2023 October 4; in original form 2023 July 4

ABSTRACT

We have selected galaxies with very high levels of Hα emission (EQW(Hα) >700 Å.) in their central regions from the final data release of the MaNGA survey. Our study focuses on 14 very well-resolved nearby galaxies with stellar masses in the range $9.5 < \log M_*/(M_\odot) < 11.5$. We investigate a variety of procedures for selecting galaxy regions that are likely to harbour excess populations of young massive stars, finding that selection in the 2D space of extinction-corrected Hα EQW and [S III]/[S II] line ratio produces the best results. By comparing stacked spectra covering these regions with stacked spectra covering normal starburst regions with 100 Å<EQW(Hα) <200 Å, we obtain the following main results: (1) Clear signatures of excess Wolf–Rayet stars are found in half of the Hα excess regions, (2) galaxy regions containing excess Wolf–Rayet stars are more often associated with the presence of high-ionization emission lines characteristic of accreting black holes. Excess [Ne III] is detected in 4 out of 8 of the WR regions and there are tentative [Fe X] detections in 2 galaxies. (3) Regions of the galaxy with excess Wolf–Rayet stars are located where the interstellar medium has larger ionized gas turbulent velocities and higher neutral gas overdensities. We make a first attempt to constrain changes in the high-mass end of the stellar initial mass function (IMF) using the HR-pyPopStar evolutionary population synthesis models that include high-wavelength-resolution theoretical atmosphere libraries for Wolf–Rayet stars.

Key words: galaxies: nuclei – galaxies: star formation – galaxies: stellar content – stars: Wolf–Rayet – galaxies: bulges – galaxies: active.

1 INTRODUCTION

The connection between active galactic nuclei (AGN) and starbursts has been a vigorous topic of research since the 1980s. Initially, much of the debate in the field was focused on whether certain classes of AGN could be entirely powered by star formation rather than by accreting black holes. Terlevich & Melnick (1985) proposed that because the most massive stars can reach very high effective temperatures in the last stages of their evolution, ionization by a population of extreme WC or WO Wolf–Rayet stars could explain the observed luminosities of high ionization lines such as [O III]λ5007 and [Ne III]λ3869 in Seyfert 2 galaxies, and there was therefore no need to invoke an accreting supermassive black hole as the main powering source in these systems.

Subsequent searches uncovered a handful of type 2 Seyfert galaxies with very strong Wolf–Rayet star signatures, such as Markarian 477 (Heckman et al. 1997), but the spectroscopic signatures of young stellar populations in most objects tended to be much weaker (Gonzalez Delgado et al. 1998, Cid Fernandes et al. 2001, Ho et al. 1997) and were generally in the form of large far-IR luminosities, high near-UV surface brightnesses and emission line ratios intermediate between pure type 2 Seyfert galaxies and starbursts. As a result, the Seyfert galaxy unification scheme introduced by Antonucci (1993) in which viewing angle was the main factor in whether an AGN had a Type I and Type II spectrum, became widely accepted and the Wolf–Rayet star scenario dropped out of fashion.

The next insight into the role of star formation in the AGN phenomenon was associated with the era of large surveys of galaxies, such as the Sloan Digital Sky Survey (SDSS; York et al. 2000), where AGN could be selected using optical line ratio diagnostic diagrams (Kauffmann et al. 2003, Kewley et al. 2006), as well as large samples of X-ray and IR-selected AGN in the redshift range 0.2–2.5 (e.g. Mendez et al. 2013; Stern 2015; Brown et al. 2019). Heckman & Kauffmann (2004) estimated the volume-averaged ratio of star formation to black hole mass accretion in galaxies and found that for early-type galaxies with black hole masses in the range $10^7 - 10^{8.5}\,M_\odot$, this value was around 1000, in good agreement with the empirically derived ratio of bulge mass to black hole mass in nearby galaxies (Marconi & Hunt 2003; Häring & Rix 2004). This result appeared to suggest a close relationship between star formation in the bulge and the fuelling/growth of supermassive black holes.

Later work showed that this relationship derived by integrating the total star formation and black hole growth rates over large populations

★ E-mail: gamk@mpa-garching.mpg.de

of objects, does not extend in a simple way to individual systems. Kauffmann & Heckman (2009) analysed the observed distribution of Eddington ratios in galaxies split into bins of black hole mass and showed that in objects with young stellar populations, the Eddington ratio distribution was characterized by a broad lognormal distribution of accretion rates peaked at a few per cent of the Eddington limit. Moreover, the distribution depended very little on the central stellar population of the galaxy, as characterized by its 4000 Å break strength. In this work, the Eddington ratios were estimated using the [O III] line luminosity. A subsequent analysis used X-ray luminosity as a black hole accretion rate indicator and IR luminosity to measure star formation rate, and reached very similar conclusions (Stanley et al. 2015). A reservoir of gas in the host galaxy is clearly necessary for both ongoing star formation and black hole growth, but does not closely regulate the latter.

Attention in the field has now turned back to asking whether there are particular interstellar medium conditions or configurations that are favourable to the initial formation of a supermassive black hole in a galaxy or a major change in its mass over a short-time interval. The compression of gas during the merging of galaxies has long been hypothesized to be an important mechanism to fuel the brightest AGN in the universe (Sanders et al. 1988). Once again, a clear link between AGN and merging galaxies has not held up under careful statistical investigation (e.g. Li et al. 2008; Reichard et al. 2009; Kocevski et al. 2012). Alternatively, mergers are not the only mechanism that cause gas compression in galaxies. Black hole accretion is a process that occurs on very small scales and it is likely that local interstellar medium conditions need to be measured to find the clearest AGN–starburst connections.

The SDSS-IV included a survey called MaNGA (Mapping Nearby Galaxies at APO), which obtained spectral measurements across the face of each of ∼10 000 nearby galaxies thanks to 17 simultaneous integral field units (IFUs) (Bundy et al. 2015, Yan et al. 2016). In a number of papers, AGN have been identified using neubular emission line ratio diagnostics (Baldwin, Phillips & Terlevich 1981; hereafter BPT) and their resolved star formation profiles have been studied. The main conclusion from these studies is that BPT-selected AGN have suppressed central star formation rates compared to control samples matched in stellar mass and redshift (Guo et al. 2019; Jin et al. 2021; Lammers et al. 2023), leading to the conclusion that AGN have acted to quench star formation in galaxies from 'inside-out'. Other studies have focused on searching for 'hidden' populations of accreting black holes in more strongly star-forming galaxies using weaker, but higher-ionization emission lines such as [Ne V]λ3427 (Negus et al. 2023) or He II λ4686 (Tozzi et al. 2023). These galaxies are hypothesized to be at an earlier stage of an accretion event onto the black hole, when active star formation is still ongoing.

Our previous work has focused on the hypothesis that black holes may form and accrete in environments that are unusually rich in very young, massive stars. We initially focused on selecting galaxies with extinction-corrected H α equivalent widths too large to be explained with a standard initial mass function (IMF). In a study of these galaxies in an early data release of the SDSS-IV MaNGA survey (Aguado et al. 2019), Kauffmann (2021) found that the 4000 Å break is either flat or rising towards the centre of the galaxy, indicating that the central regions host evolved stars, but the H α equivalent width also rises steeply in the central regions, a trend that cannot be explained by any star formation history assuming a standard IMF. The implication is that there is an excess of ionizing sources near the centres of these galaxies.

Subsequent work (Kauffmann et al. 2022) focused on clarifying the nature of the ionizing sources in very high H α equivalent width galaxies in a much larger sample selected from the SDSS main sample with single-fibre rather than IFU spectra. This study found [Ne V] emission in a subset of the H α excess galaxies with radio detections indicating that accreting black holes were likely present in a subet of the objects. It also revealed strong and broadened He IIλ4686 emission lines characteristic of stars from the WN sequence Wolf–Rayet stars in some of the galaxies. Because the signal-to-noise of the single fibre SDSS spectra is low compared to MaNGA (1 h exposures compared to 3 h exposures on the APO 2.5-m telescope), the analysis could only be carried out for stacked spectra of a few dozen galaxies. Even so, the stacked spectra were too low in *S*/*N* to detect the high-ionization (C III and C IV) lines associated with WC sequence Wolf–Rayet stars. The study could also not focus on local interstellar medium conditions within individual galaxies.

In this paper, we return to samples of H α excess galaxies selected from the final release of the MaNGA survey (Abdurro'uf et al. 2022). Our study focuses on well-resolved nearby galaxies with stellar masses in the range $9.5 < \log M_*/(M_\odot) < 11.5$, that is, within a factor of 10–20 the mass of our own Milky Way, which is estimated as $6 \times 10^{10}\, M_\odot$ (Licquia & Newman 2015). We refine our procedures for selecting galaxy regions that are likely to harbour excess populations of young massive stars. We compare stacked spaxel spectra of these regions with stacked spaxel spectra of more normal star-forming regions within the same galaxy. Finally, we make a first attempt to constrain changes in the high-mass end of the stellar IMF using the HR-pyPopStar evolutionary population synthesis models that include high-wavelength-resolution theoretical atmosphere libraries for Wolf–Rayet stars (Millán-Irigoyen et al. 2021).

Our paper is organized as follows. In Section 2, we describe how the galaxy sample analysed in this paper is selected. In Section 3, we discuss our spaxel selection and stacking procedure. Section 4 presents two-dimensional maps of physical properties derived from individual spaxels. Sections 5 and 6 present results on Wolf–Rayet features and high-ionization emission lines, while Section 7 focuses on interstellar medium properties. Section 8 explores the effect of IMF changes predicted by the HR-pyPopStar models. A summary and discussion of the main results is presented in Section 9.

2 THE PARENT GALAXY SAMPLE

The galaxies are selected from the MaNGA DRPALL file, which provides basic photometric information and physical quantities such as stellar mass for the 10 010 unique galaxies with data cubes available as part of the final MaNGA data release (DR17). Most of the galaxy properties in the files are taken from the NASA-Sloan Atlas (NSA) catalogue, a catalogue of images and parameters of local galaxies derived from SDSS imaging. The object detection, deblending, and other details regarding the image analysis can be found in Blanton et al. (2011). The image analysis is better tuned for large, bright galaxies than the standard SDSS processing.

We apply a cut on the ratio of the galaxy major-to-minor axis lengths $b/a > 0.75$ to select face-on systems, a cut on stellar mass $9.5 < \log M_*/(M_\odot) < 11.5$ to select galaxies within a factor of 10 the mass of our own Milky Way, and a redshift cut $0.005 < z < 0.05$ to select the most nearby systems with better-resolved coverage of the inner stellar population. This procedure yields 1858 data cubes that are listed as having high-quality data.

The MaNGA data-analysis pipeline (MaNGA DAP, Westfall et al. 2019) is the survey-led software package that analyses the data produced by the MaNGA data-reduction pipeline (MaNGA DRP, Law et al. 2016) to produce physical properties derived from MaNGA spectroscopy. The DAP output primarily consists of two

Table 1. Table of physical quantities for the Hα excess samples studied in this paper (top: 8 galaxies with WR detections, bottom: 6 galaxies with no WR detections) The columns are as follows: (1) MaNGA identifier (plate ID), (2) MaNGA identifier (IFU design number), (3) right ascension (J2000), (4) declination (J2000), (5) redshift, (6) NUV-r colour, (7) r-band half-light radius (arcsec), (8) axial ratio b/a, (9) Sersic index, (10) logarithm of the stellar mass ($M_{\odot}$), (11) number of spaxels within $0.15R_{50}$, and (12) number of spaxels within $0.5R_{50}$.

Plate ID	IFU design number	RA	Dec.	z	NUV-r	r50	b/a	Sersic index	log (M_*)	$N_{spax}(0.15R_{50})$	$N_{spax}(0.5R_{50})$
10509	12703	168.545376	48.318516	0.007122	3.224800	20.110100	0.806780	1.633650	10.353810	113	1273
7959	6103	256.283191	30.403216	0.034064	5.155600	6.317760	0.958269	5.404750	10.575510	29	325
8154	12701	45.435110	-0.592630	0.031465	2.642700	10.275900	0.842325	0.512912	10.237617	30	335
8260	9101	182.286727	44.003165	0.037542	2.741300	8.080410	0.761730	1.528640	10.594678	21	241
8311	6104	205.282731	23.282055	0.026353	3.311900	5.444330	0.835267	1.871530	10.283634	9	97
9093	12705	242.406339	28.051843	0.032796	2.225500	7.815390	0.843981	1.068260	10.116239	21	193
9494	9102	127.434839	22.424396	0.025005	2.177800	6.606660	0.783767	1.501930	10.062650	9	137
9507	12704	129.600037	25.754501	0.018181	3.152400	7.900920	0.850208	1.847050	10.185556	21	193
11748	12705	138.748621	29.730240	0.021161	4.299219	8.687565	0.824277	5.669246	10.676188	21	241
11830	12701	195.920019	51.495081	0.038110	3.037155	7.566992	0.755167	1.589030	10.346302	21	277
8149	3704	120.207222	27.500359	0.017345	2.116600	7.544130	0.843134	0.790922	9.994284	29	321
8336	12704	210.597154	38.710223	0.019987	4.052200	10.364800	0.875560	2.614080	10.098990	29	341
8465	9102	198.189163	46.934987	0.027681	3.901800	7.458280	0.837129	3.513580	10.061317	21	241
8595	3703	221.437984	51.580820	0.029627	3.798600	7.070540	0.884235	4.139190	10.585714	13	153

output files, the MAPS and model LOGCUBE files, provided for each combination of PLATE-IFU and DAPTYPE. The MAPS file provides 2D 'maps' (i.e. images) of DAP measured properties, such as the fluxes and equivalent widths of emission lines, absorption line spectral indices and stellar kinematic quantities such as V and σ. We note that the instrumental spectral line-spread function (LSF) typically has a 1σ width of about 70 km s^{-1} (Law et al. 2021). To select galaxies with excess Hα emission, we make use of the Hα and Hβ flux and continuum measurement maps provided by the HYB10-MILESHC-MASTARSSP MAP files. In these files, the stellar-continuum measurements are made from spectra binned to S/N ~10 using a Voronoi binning algorithm, but the emission-line measurements are performed on the individual spaxels, yielding the highest possible spatial resolution for these measurements.

We use the MAPS files to calculate the average extinction-corrected Hα equivalent width in 10 equally spaced radial bins from 0.025 to 0.5 R_{50}, where R_{50} is the r-band half-light radius provided by the DRPALL file. We adopt the same procedure for extinction correction using the Balmer decrement Hα/Hβ described in Kauffmann (2021) and we retain 58 galaxies where at least one radial bin has an average Hα EQW greater than 700, placing it into the category of Hα excess systems, where the extinction-corrected line strength is a factor of two higher than that predicted for a starburst of zero age with a standard Kroupa (2001) or Chabrier (2003) IMF (see Kauffmann (2021) for more details). We select 17 galaxies with the best spatially resolved observations, defined as the number of spaxels within the very central region of the galaxy ($R < 0.15R_{50}$).

Table 1 lists some of the key properties of the galaxies that form part of the study in this paper. These include the MaNGA identifier, position, redshift, NUV-r colour, half-light radius R_{50}, axial ratio (b/a), Sersic index, and stellar mass. In addition, we list the number of spaxels included within $0.15R_{50}$ and $0.5R_{50}$. Physical properties are listed for the sample with clearly detected Wolf–Rayet features and the sample with no detected features in separate sections of the table. The three galaxies that are are not listed in the table are classified as weak detections and do not form part of the analysis. The Wolf–Rayet feature detection procedure and classification will be discussed in more detail in the next section.

We note the galaxies in this sample have R_{50} values between 5 and 20 arcsec. Table 1 shows that for the selected sample, the region $R < 0.5R_{50}$ is typically covered by 200–300 spaxels and the very central region of the galaxy $R < 0.15R_{50}$ is covered by 10–30 spaxels. As we will show, stacking of subsets of very high Hα EQW spaxel spectra in the galaxy and comparing these spectra with stacked spectra of spaxels in ordinary starburst regions is useful for pulling out even relatively weak Wolf–Rayet features.

All the galaxies in both the Wolf–Rayet detected and non-detected subsamples have stellar masses in the range $\log M_*/(M_{\odot}) = 10 - 10.6$. Kauffmann et al. (2022) extracted a sample of 1000 Hα excess galaxies from the SDSS main sample with single fibre spectra and showed that the stellar mass distribution of galaxies with Hα excess peaks in the range $10^{10} - 10^{10.5}\,M_{\odot}$.

With one exception, the Sersic indices in the Wolf–Rayet sample are below 2, indicating that they are late-type spiral systems. 4 out of 6 of the galaxies without Wolf–Rayet feature detections have Sersic indices greater than 2, indicating the stellar light in these systems is more concentrated. We note that the Kauffmann et al. (2022) study only detected Wolf–Rayet features in stacked spectra of many galaxies rather than in individual galaxies, so it was not possible to investigate systematic changes in galaxy morphology.

Figs 1 and 2 present SDSS g, r, i-band postage stamp images of the two subsamples with and without Wolf–Rayet detections. In addition, we also show VLA FIRST 1.4 GHz cut-out images of all the sources. Both subsamples contain one galaxy merger (9507.12704 and 11830.12701). The Wolf–Rayet detected subsample contains 2 galaxies with close companions (7959.6103 and 8311.6104). Both subsamples also contain galaxies where there is no clear perturber. In the cases where there is a high-S/N radio detection, the radio emission appears to be unresolved in most cases. Occasionally, the radio emission is significantly offset from the centre of the galaxy (e.g. 8336.12704). At the resolution of the VLA images, the radio properties or evidence of mergers/interactions do not provide a clear predictor of whether or not Wolf–Rayet features will be detected in the spectra.

3 SELECTION OF SPAXELS AND STACKING PROCEDURE

Early attempts to find Wolf–Rayet galaxies relied on imaging strongly star-forming systems with a narrowband λ4684 filter (Drissen et al. 1990, Sargent & Filippenko et al. 1991). Catalogues of Wolf–Rayet galaxies were compiled by a number of authors as

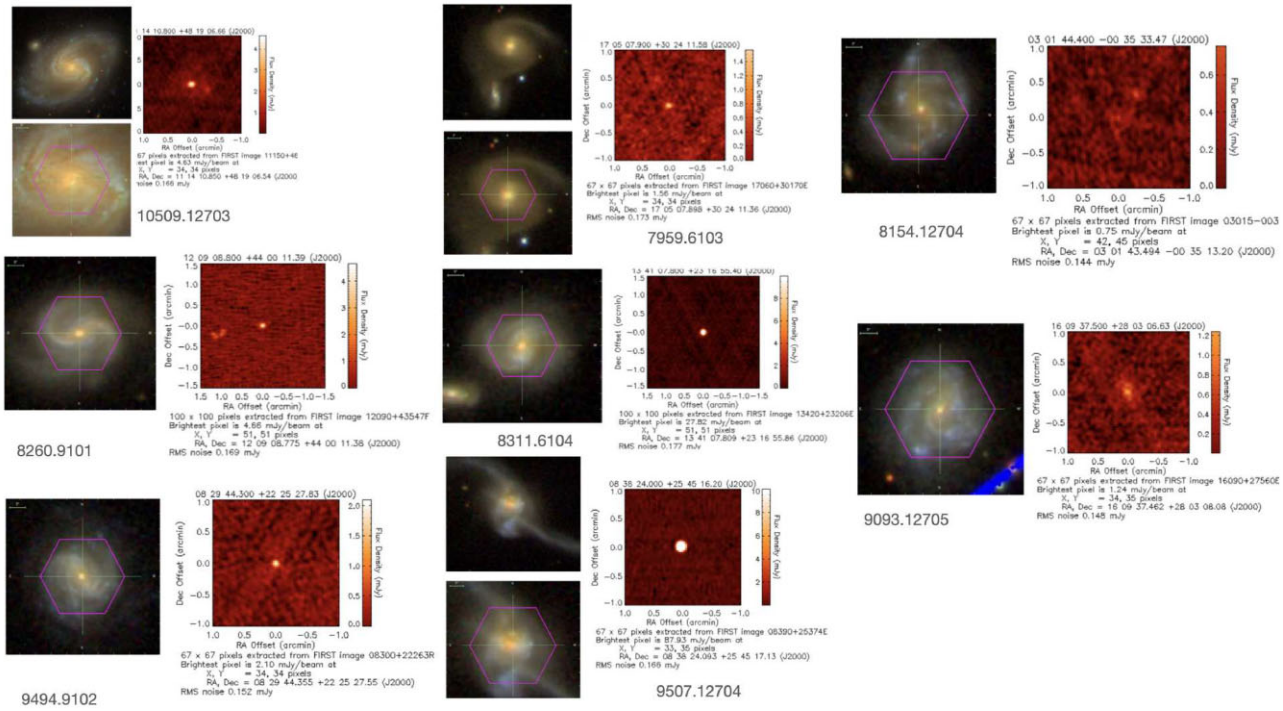

Figure 1. A gallery of SDSS *g*, *r*, *i*, and VLA FIRST 1.4 GHz postage stamp images of the 8 galaxies with Wolf–Rayet feature detections.

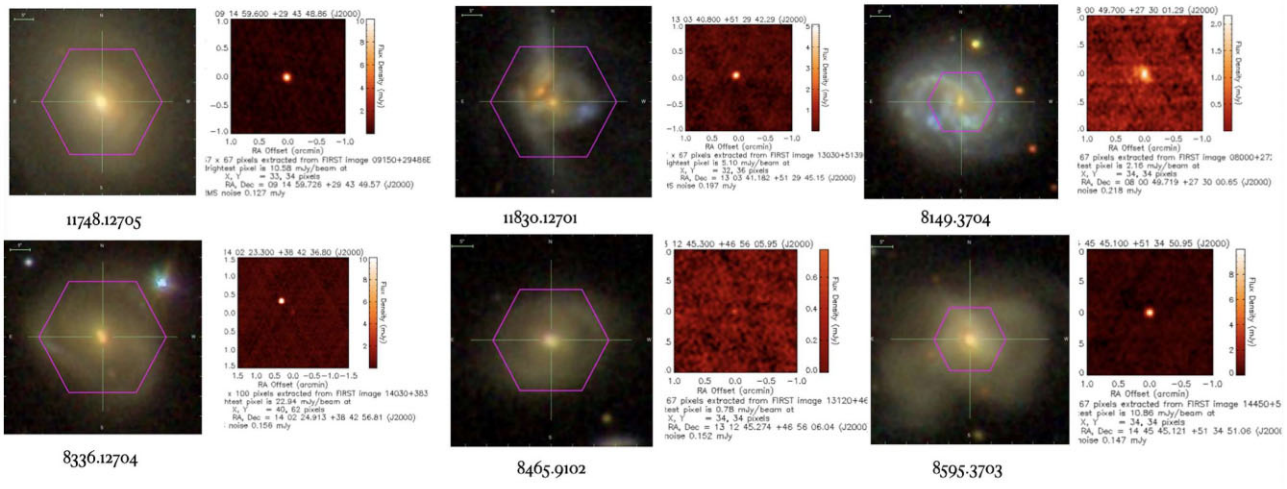

Figure 2. A gallery of SDSS *g*, *r*, *i*, and VLA FIRST 1.4 GHz postage stamp images of the 6 galaxies with no Wolf–Rayet feature detections.

more and more objects were discovered (e.g. Conti 1991, Schaerer et al. 1999, Guseva et al. 2000) In recent years, searching for Wolf–Rayet features in spectra obtained as part of large galaxy surveys has become the norm. Catalogues constructed from single-fibre observations of galaxies from the SDSS have been constructed by first pre-selecting stronger emission line objects based on their measured H β (Brinchmann et al. 2008) or Hϵ equivalent widths (Zhang et al. 2007) to select the strongest star-forming systems and then searching for a broad emission features (blue bump) in the vicinity of 4650 Å. Such techniques were extended to individual spaxel spectra in IFU observations of galaxies obtained as part of the MaNGA survey by Liang et al. (2020). Miralles-Caballero et al. (2016) identified extragalactic regions with Wolf–Rayet stars in IFU spectra obtained by the Calar Alto Legacy Integral Field Area (CALIFA) survey (Sánchez et al. 2012). Their search algorithm selected spaxels with large H α equivalent widths, subtracting a best fit continuum model and then applying a pseudo-filter spanning the wavelength range 4600–4700 Å. A similar procedure was applied to detect the red bump.

In this paper, we introduce a spectrum stacking technique to increase the signal-to-noise of the resulting spectra. Rather than searching for pre-defined specific features in individual spaxel spectra, we proceed by comparing stacked spectra in regions where ionized gas indicators indicate that the local density of massive stars is unusually high with stacked spaxel spectra from more normal regions within the same galaxy. This technique has the advantage

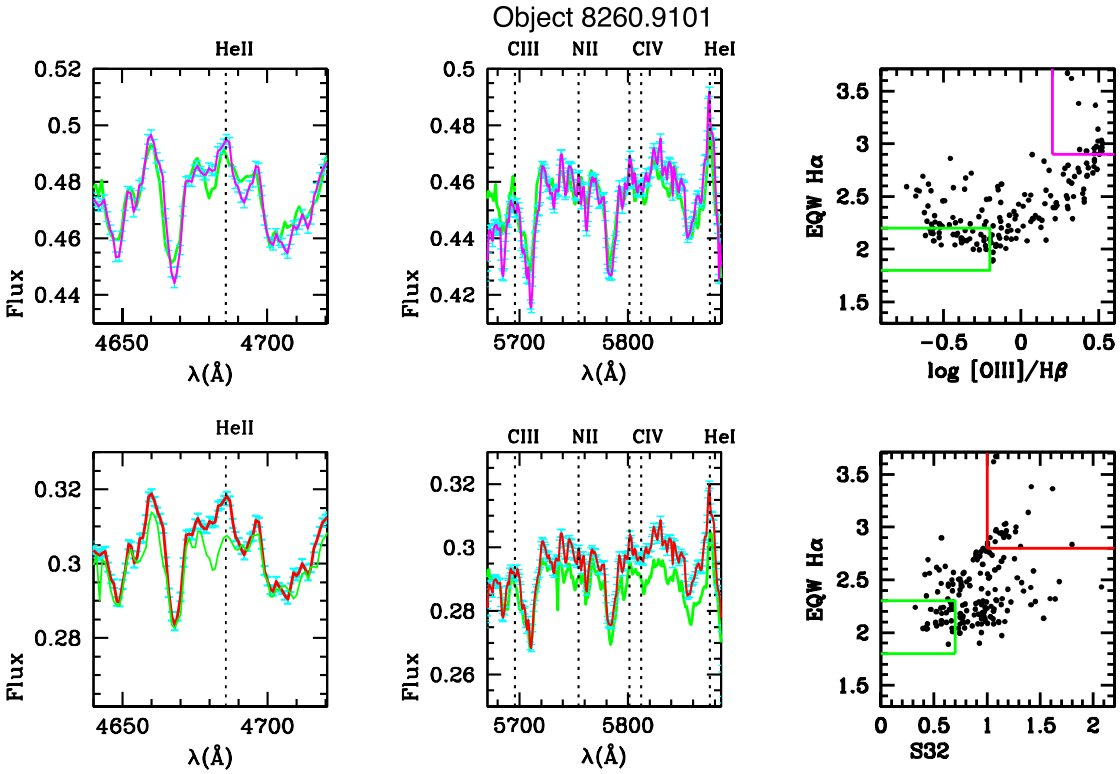

Figure 3. An example where selection of spaxels in the plane of EQW Hα versus S32 (see bottom panels) leads to stronger WR features than selection in the plane of EQW Hα versus [O III]/Hβ (see top panels). The blue bump region is plotted in the left panels and the red bump region in the right planels. The red, magenta and green lines show the stacked spectra for the spaxels with emission line measurements located in the red,magenta and green bounding boxes indicated in the right-hand panels (see explanation in text for bounding boxes). The spectra plotted in green indicate 'normal starburst' regions of the galaxy, whereas the spectra plotted in red and magenta indicate regions with high Hα equivalent width and high ionization. The 1σ measurement errors on the red and magenta stacked spectra are plotted in cyan.

of increasing the signal-to-noise in the spectra that we analyse and enables us to look for weak features associated with other correlated phenomena, such as emission from accreting black holes that are hidden within the starburst (Kauffmann et al. 2022). The inner regions of strongly star-forming galaxies also contain a lot of dust and as we will show, interstellar absorption features are very strong and this can also hinder accurate characterization of the stellar continuum that is necessary to dig out the weaker emission lines.

Our technique could have the disadvantage that because the pre-selection is based on emission line properties, areas of the galaxy where Wolf–Rayet stars are not correlated with a high density of ionized gas may be missed. Because the spatial resolution in MaNGA is quite low and the regions that we are picking out for stacking typically extend over a contiguous region of a few hundred parsecs to a kiloparsec, we believe this is unlikely to be a major problem. We speculate that this may be more of an issue in the outer discs of star bursting galaxies, which often contain isolated, compact clumps of very young stars embedded in a surround lower density interstellar medium.

We experimented with a variety of strategies for spaxel stacking with view to extracting visible Wolf–Rayet features in our central galaxy spectra. The strategies can be summarized as follows: (1) stack spectra with the highest extinction-corrected Hα equivalent widths, (2) stack spectra selected both by extinction-corrected Hα equivalent width and a measure of the ionization state of the gas. In star-forming galaxies, ionizing photons are produced by the most massive stars that are present and the ionization parameter provides an independent indicator of the local surface density of young massive stars.

There are a number of line ratios that are commonly used as diagnostics of the ionization state of the photo-ionized gas in the interstellar medium of galaxies. [O III]λ5007/[O II]λ3727 is strongly affected by dust reddening and is not considered in this work. [O III]λ5007/Hβ has the advantage that the lines are very closely spaced so that dust reddening effects are minimized, but this ratio is strongly dependent on metallicity. In recent work, Sanders et al. (2020) introduce the line ratio S_{32} = [S III]$\lambda\lambda$9069, 9531/[S II]$\lambda\lambda$6716, 6731 as an ionization diagnostic. Since the lines are located at relatively long wavelengths, this ratio is not very sensitive to dust and CLOUDY models (Ferland et al. 1998,2017) indicate that it is even more weakly dependent on metallicity than [O III]λ5007/[O II]λ3727.

By trying out different methodologies, we find that a spaxel cut in the 2D space of Hα equivalent width and ionization parameter is better at picking out Wolf–Rayet feratures than a cut on Hα equivalent width alone. This probably indicates that the dust corrections that we apply to deredden EQW Hα are not fully accurate. We also find that cuts using EQW Hα and S_{32} sometimes work better than cuts on EQW Hα and [O III]/Hβ. An example of such a case is shown in Fig. 3. The upper right panel shows the spaxels selected for stacking in the plane of EQW Hα versus [O III]/Hβ. The spectra from the spaxels with measurements falling within the magenta box are combined to form the spectra plotted in magenta in the middle and top-left panels. We normalize each spectrum to the average

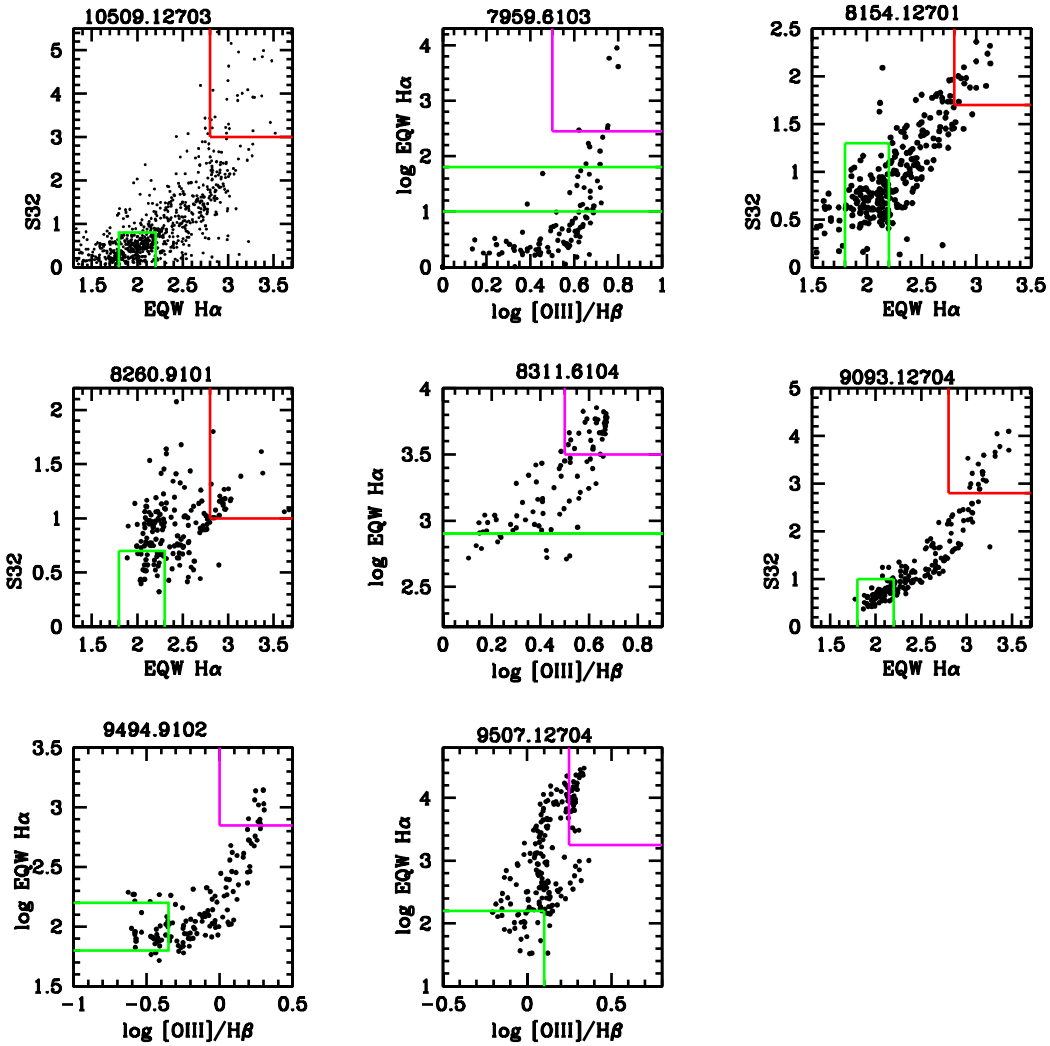

Figure 4. The selection of spaxels in the plane of EQW H α versus S32 or EQW H α versus [O III]/H β is shown for all 8 objects with WR feature detections.

flux integrated over the wavelength range 5345–5410 Å which is free of emission lines and strong absorption features. The spectra from the spaxels with measurements falling within the green box are stacked to show the spectra of 'normal starburst' regions of the galaxy for comparison. Comparison of the stacked spectra over the wavelength regions covering the He II λ4686 and C IV λ5801 emission lines are used to select galaxies with detectable Wolf–Rayet excess.

The top panels of Fig. 3 show that for the galaxy 8260.9101 there is marginally significant difference ($<2\sigma$ in the region of the emission lines) between the two spectra if spaxels are selected using the [O III]/H β ratio. This system would be classified as a weak detection. The bottom panels of Fig. 3 show what happens if the same exercise carried out in the plane of EQW H α versus S_{32}. The spaxel measurements bifurcate into two tracks in this plane – one where there is no clear relation between EQW H α and S_{32} and another track where there is a clear correlation. Stacking the high EQW H α spaxels from this second track now yields spectra with clear excess He II λ4686 and C IV λ5801 emission, so the galaxy is now classified as a detection.

In Fig. 4, we show the spaxel selection boxes for all eight of the galaxies with Wolf–Rayet excesses. The spaxel selection boxes for the high ionization stacks are chosen so that they contain 1–2 dozen spaxels with the highest H α equivalent widths and the highest ionization parameters. The green selection boxes are chosen to cover spaxels in the H α equivalent width range 80–200 Å with the lowest ionization parameters. These values are chosen because this is the expected value for a starburst galaxy with a normal IMF (see for example Fig. 10 in Kauffmann (2021)). In two cases (8311.6104 and 7959.6103), we are forced to change the spaxel selection boundaries because there only a few spaxels with EQW(H α) in the range 80–200 Å.

In 4 out of the 8 cases, the EQW H α versus S_{32} cut yields stronger excess He II λ4686 and/or C IV λ5801 emission and is adopted as our default. In the cases where [O III]/H β selection is adopted, S_{32} almost always yields very similar (i.e. not worse) results. The corresponding spectra in the blue and red bump wavelength regions are presented in Figs 8 and 9and are discussed in Section 5. We note that our Wolf–Rayet detection fraction of 50 per cent in H α excess galaxies is very high compared to what is obtained for the star-forming galaxy population as a whole. Liang et al. (2020) derive a Wolf–Rayet detection fraction in star-forming MaNGA galaxies that increases towards lower stellar masses, peaking at a value of 12 per cent at $\log M_* \sim 10^{9.75}\, M_\odot$.

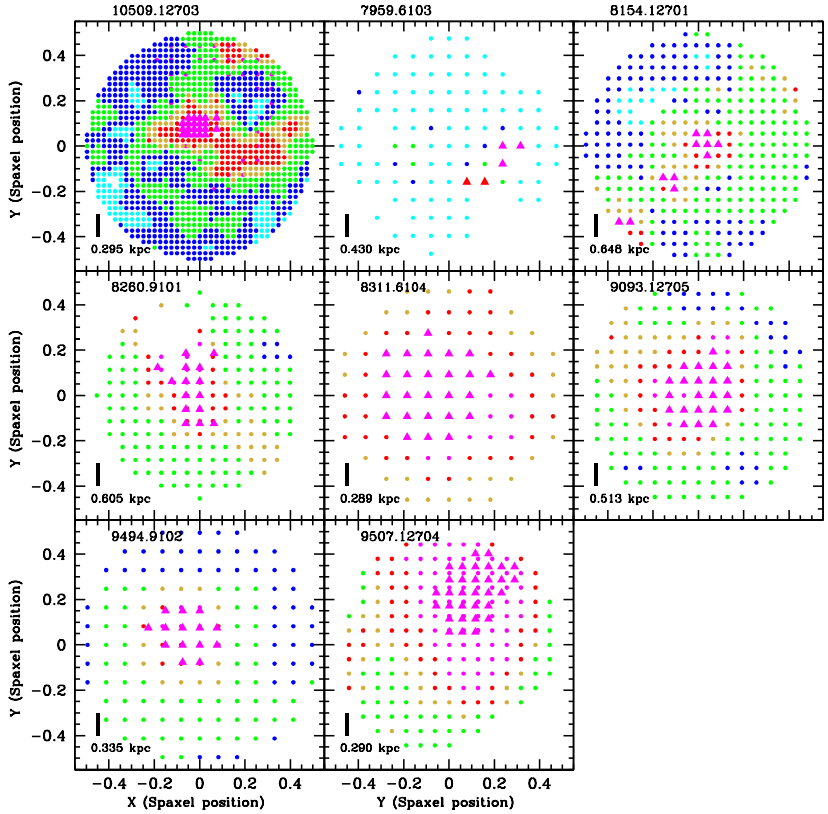

Figure 5. Two-dimensional maps of H α equivalent width measurements for the 8 galaxies with Wolf–Rayet detections. The circular points indicate each spaxel measurement and are colour-coded as follows: magenta (EQW(H α) >3.0), red (2.5<EQW(H α) <3.0), dark gold (2.0<EQW(H α) <2.5), blue(1.5<EQW(H α) <2.0), and cyan(EQW(H α) <1.5). The triangular points colour-coded in magenta indicate those spaxels that were stacked to produce the spectra with detectable WR excess. The X and Y-axes are in units of the the scaled radius measured in the *r*-band, with a value 0.5 indicating the half-light radius. A bar is provided at the bottom-left of each panel that can be used to calibrate the physical size of the regions under study.

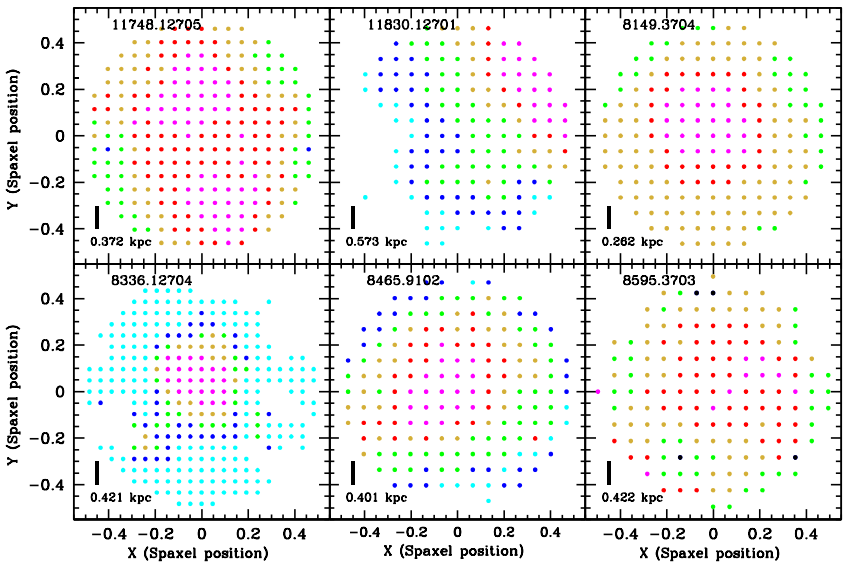

Figure 6. As in the previous figure, except for the 6 galaxies with no Wolf–Rayet detections.

4 MAPS OF SPECTRAL QUANTITIES

Figs 5–8 present two-dimensional maps showing how the dust-corrected H α equivalent width and ionization parameter [O III]/H β vary within the half-light radius R_{50}. The maps have all been scaled to the half-light radius of each object (see caption of Fig. 5 for more details). Results are shown separately for the 8 galaxies with Wolf–Rayet excess detections and the 6 galaxies with no Wolf–Rayet excess. In Fig. 5, we indicate the spaxels that are included in the stacked spectra with Wolf–Rayet excess using large magenta

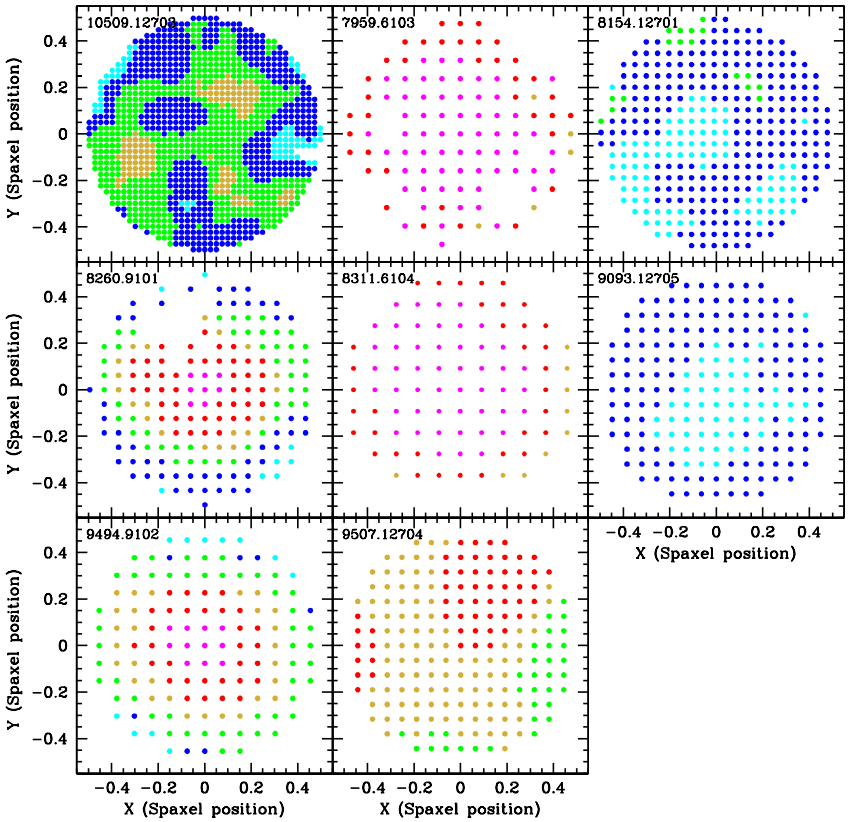

Figure 7. Two-dimensional maps of [O III]/H β measurements for the 8 galaxies with Wolf–Rayet detections. The circular points indicate each spaxel measurement and are colour-coded as follows: magenta log ([O III]/H β >0.6), red (0.4<log [O III]/H β) <0.6), dark gold (0.1<log [O III]/H β) <0.4), green (–0.3<log [O III]/H β) <0.1), blue (–0.5<log [O III]/H β) <–0.3), and cyan (–0.8<log [O III]/H β) <–0.5).

triangles. As can be seen, these spaxels are sometimes, but not always located near the very central regions of the galaxy. In 2 out of 8 galaxies, the stacked spectra include spaxels that extend as far as the *r*-band half-light radius R_{50} and in two galaxies, the stacked spaxels do not include the very central regions. The Wolf–Rayet emission is strongly offset in objects 7959.6103, 9507.12704 and weakly offset in 10509.12703. In objects 8154.12701, 8260.9101, and 9507.12704, it is exhibits a strongly asymmetric morphology with the spaxels aligned along a particular direction. In object 8154.12701, the directional alignment is so pronounced that one might hypothesize that the Wolf–Rayet emitting regions are tracing an interstellar medium component that has been shocked and compressed by a jet.

Comparison of Figs 5 and 6do not reveal clear differences. This means that the H α emission is distributed much the same way in the two subsamples with and without WR features. A bar is provided at the bottom left of each panel that can be used to calibrate the physical size of the Wolf–Rayet regions under study. The sizes range from 300 pc to over 1 kpc.

Comparison of Figs 7 and 8 indicates that the galaxies with Wolf–Rayet excess emission usually have more highly ionized gas within R_{50}. In the Wolf–Rayet excess subsample, 5 out of 8 galaxies have spaxels where log [O III]/H β >0.4 – these are values that are often associated with AGN. In the subsample with no Wolf–Rayet excess, only 1 galaxy out of 6 has measured [O III]/H β values this high. We note that in both subsamples the ionization parameter is usually quite uniform with occasional patches of more highly ionized gas spread throughout the central region within R_{50}. Only in 2 out of 8 galaxies in the WR excess sample is there a strong gradient in ionization (with higher values towards the central regions). In the sample without WR excess, there are no galaxies where the ionization parameter peaks near the galaxy centre. This disfavours a centrally located active galactic nucleus as the main source of the ionization in most of these galaxies.

In the Appendix, we show two additional sets of maps of two quantities: (a) the Balmer absorption line feature H8, which is sensitive to the age of the underlying population of older stars in the galaxy, (b) ionized gas velocity measured from the shift of the centroid of the H α emission line. No clear differences in these maps are found for the two subsamples. We do not consider ionized gas-phase metallicity in this paper. As we will show, the H α excess sample with Wolf–Rayet star detections often also exhibits signatures of ionization from accreting black holes, but the H α excess sample without Wolf–Rayet star signatures does not. This precludes a simple comparison of ionized gas-phase metallicity between the two samples.

5 WOLF–RAYET BUMP REGIONS

In this section, we present results from the stacked spectra, with emphasis on the Wolf–Rayet features and high ionization emission lines that may indicate the presence of accreting black holes. In all the plots, coloured lines indicate stacked spectra of H α excess spaxels selected in the plane of H α versus S_{32} (spectra plotted in red) or H α versus [O III]/H β (spectra plotted in magenta). The black lines indicate stacked spectra for the spaxels selected to have normal values of EQW H α.

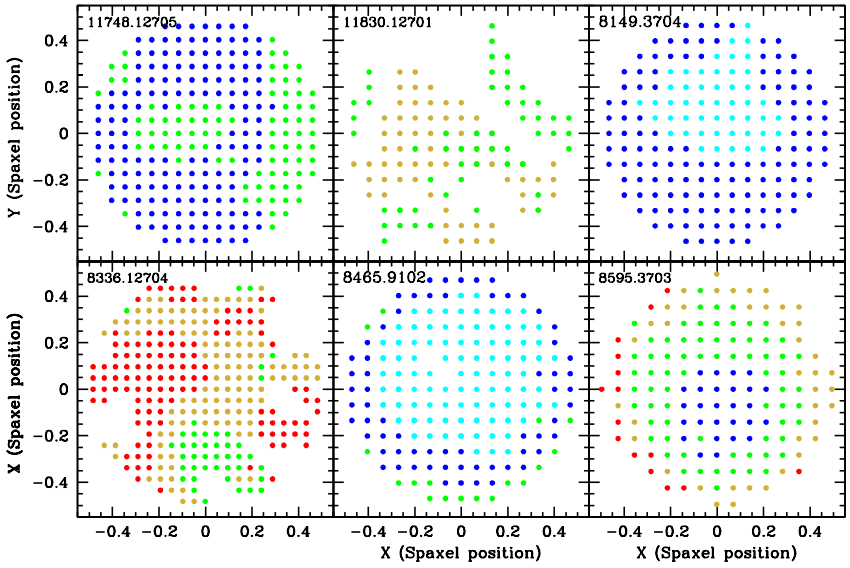

Figure 8. As in the previous figure, except for the 6 galaxies with no Wolf–Rayet detections.

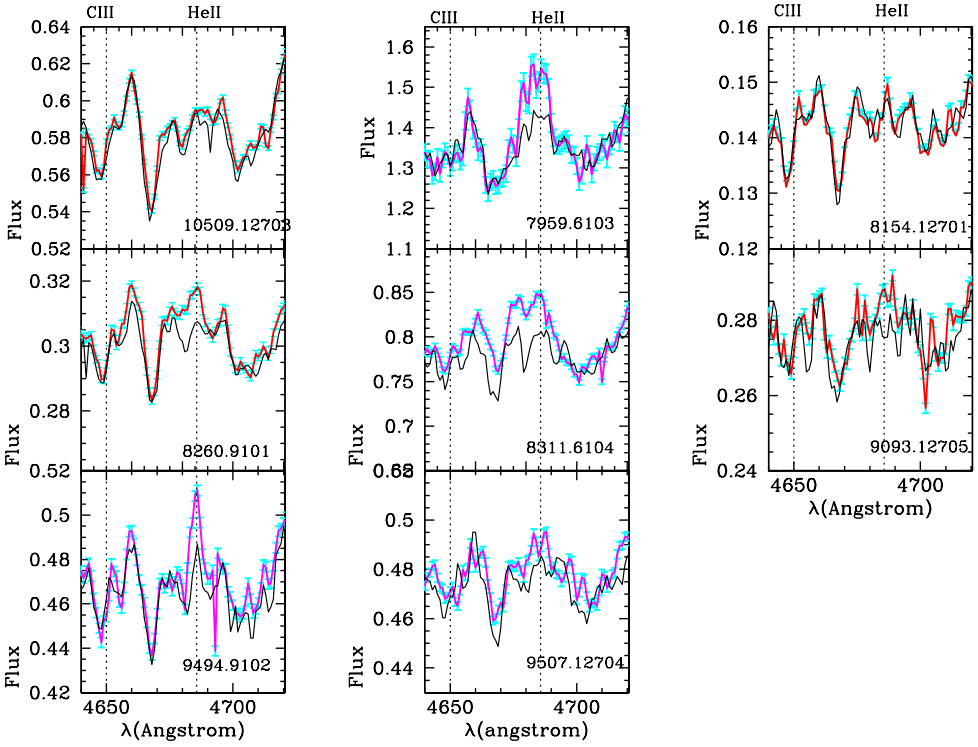

Figure 9. The 'blue bump' region of the stacked spectra is shown for the selected H α excess spaxels (red or magenta lines) compared to the spaxels with normal starburst values of the H α equivalent (black lines). Errorbars on the H α excess spectra are plotted in cyan. The spectra plotted in red are selected using a cut on S32, while the spectra plotted in magenta are selected using a cut on log [O III]/H β. The dotted lines show the location of the emission lines He II and C III as labelled on the top panels.

Fig. 9 shows the blue-bump region of the spectra. Clear broadened excess He II λ4686 emission is visible in 5 galaxies (7959.6103, 8260.9101, 8311.6104, 9093.12705, 9507.12704). The object 7959.6103 shows the strongest (> 10 per cent) excess. Objects 8260.9101, 8311.6104, 9093.12705, and 9507.12704 show smaller broad line excesses in the range 3–5 per cent. Strong narrow line excess He II λ4686 emission is visible in one object 9494.9102. Galaxies 10509.12703 and 8154.12701 exhibit little or no excess emission around the He II λ4686 line, but both objects exhibit very clear excesses in the red bump region of the spectrum, so they are included in our list of galaxies with Wolf–Rayet feature detections.

Fig. 10 shows the red-bump region of the spectra. C IV λ5801 is the clearest Wolf–Rayet emission line feature in this wavelength range and is clearly in excess in objects 10509.12703, 8154.12701, 8260.9101, 8311.6104, 9494.9102, and 9507.12704.

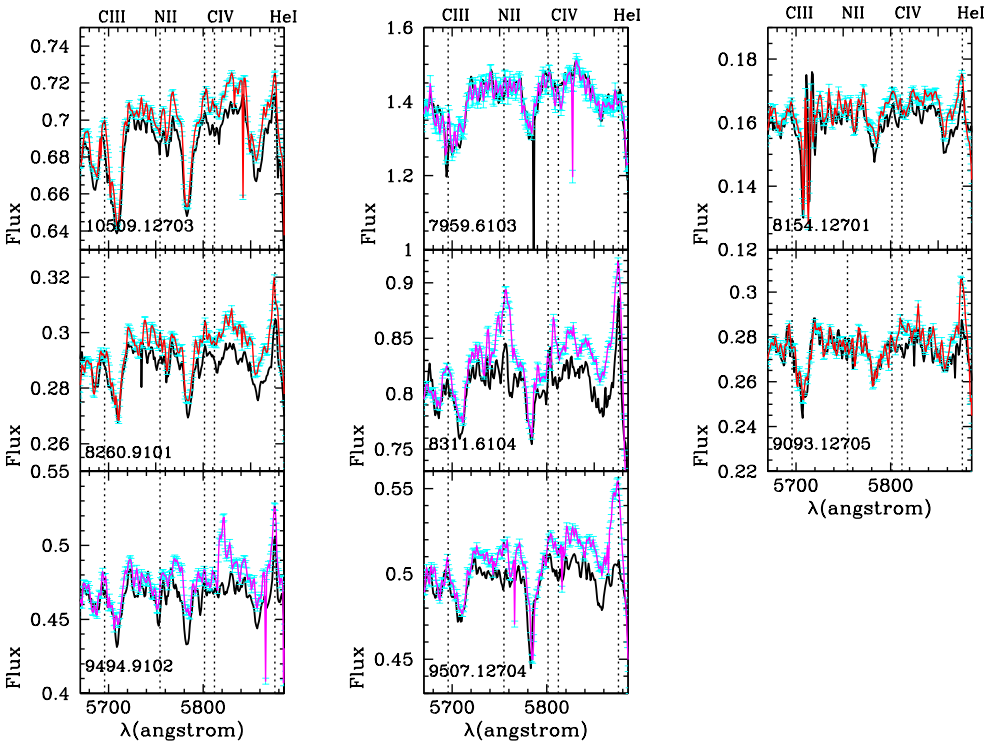

Figure 10. As in the previous figure, except for the 'red bump' region of the stacked spectra.

Excess CIIIλ5696 is also sometimes seen, but less frequently than C IV λ5801. Unlike the blue-bump excess, which is confined almost entirely to a narrow wavelength interval around the He II λ4686 emission lines, the excess red bump emission extends over a wavelength interval of 100–150 Å in most galaxies and the typical flux enhancement is at the 3–5 per cent level across this region. As we will discuss in the next section, not all the excess emission may be of stellar origin, because there are clear indications for very high ionization lines in some galaxies that are generally believed to be signatures of excitation of gas around accreting black holes.

In Appendix B, Figs B1 and B2 show stacked spectra in the blue and red bump wavelength regions for the subsample listed in Table 1 as having no excess WR feature detections. In these objects, the emission close to the He II λ4686 or the C IV λ5801 lines is the same in the stacked H α excess spectrum and in the stacked spectrum of the normal star-forming regions to within 2σ.

6 HIGHER-IONIZATION EMISSION LINES INDICATIVE OF ACCRETING BLACK HOLES

Figs 11 and 12show the regions of the spectrum covering some of the Balmer absorption line features and the high-excitation [Ne III]λ3869 emission line. for the 8 galaxies with Wolf–Rayet feature detections (Fig. 11) and the 6 galaxies without detections (Fig. 12). Neon is produced during the late stages of massive stellar evolution, by carbon burning and is expected to closely track oxygen abundance. Compared to doubly ionized Oxygen, which has an ionization potention of 35.12 eV, doubly ionized Neon with its ionization potential of 40.96 eV will be more sensitive to the presence of higher energy ionizing photons. This sensitivity is the reason why this line is sometimes used in diagnostics distinguishing star-forming galaxies from galaxies with active galactic nucleus activity (Rola et al. 1997; Pérez-Montero et al. 2007).

In the galaxies without WR detections, the Balmer absorption features differ very little between the stacked spectra covering the H α excess and the normal starburst regions. In two objects (8149.3704 and 8465.9102), the Balmer absorption lines are weaker and there is clear emission present in the higher order Hϵ and H8 Balmer absorption features in the spectra covering the H α regions, showing that star formation activity is present. In the other objects, there are no clear differences in the Balmer absorption lines, most likely because the young ionizing stars are too heavily obscured by dust to be seen in the spectra. The [Ne III] lines are weak in all 6 galaxies without WR detections and there is no difference between the line strengths in the H α excess and normal starburst stacked spectra.

In contrast, Fig. 11 shows that the stacked spectra of the H α excess spaxels in the sample with Wolf–Rayet detections exhibit enhanced [Ne III] emission in 5 out of 8 galaxies (10509.12703, 8260.9101, 8311.6104, 9494.9102, and 9507.12704). In these galaxies, the Balmer absorption lines are often weaker, without clear indication of infilling by a narrow emission line component. If the origin of the [Ne III] excess is from AGN, it could be that the weaker Balmer emission is produced by a non-thermal component (e.g. radiation from an accretion disc).

We further investigate evidence for accreting black holes by looking for [Fe X]λ6374 coronal line emission. This transition has an ionization potential of 262.1 eV and is therefore considered a reliable signature of AGN activity in galaxies (e.g. Penston et al. 1984; Prieto & Viegas 2000). Coronal line emission can be produced either by gas photo-ionized by a hard AGN continuum (e.g. Korista & Ferland 1989; Oliva et al. 1994; Pier & Voit 1995) or mechanically excited by radiative shock waves that are driven into the host galaxy by radio jets from the AGN (Wilson & Raymond 1999). Recently, Molina et al. (2021) and Kimbro et al. (2021) have used this line as a way of searching for black holes in dwarf galaxies. In Fig. 13, we present stacked spectra from 4 galaxies where there is a clear feature

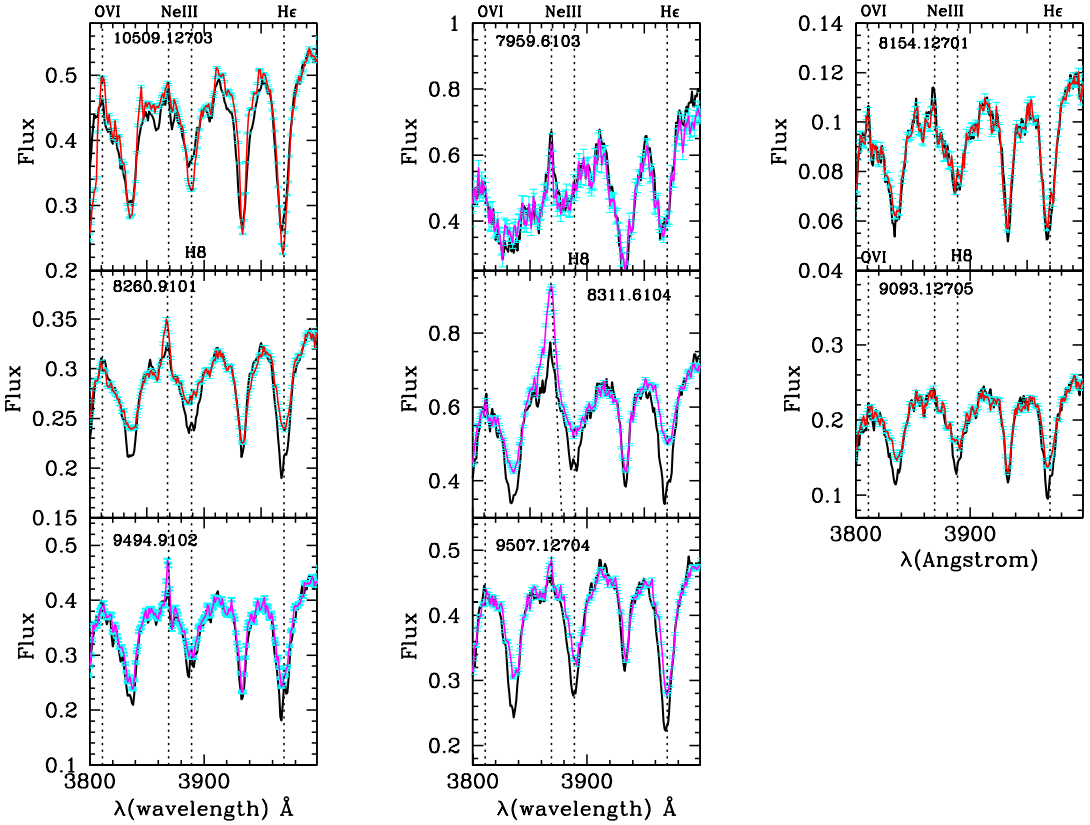

Figure 11. The Balmer absorption line region of stacked spectra from α excess spaxels (red or magenta lines) is compared to stacked spectra from spaxels with normal starburst values of the Hα equivalent width (black lines). Results are shown for the 8 galaxies with WR feature detections. Errorbars on the Hα excess spectra are plotted in cyan. The spectra plotted in red are selected using a cut on S32, while the spectra plotted in magenta are selected using a cut on log [O III]/Hβ.

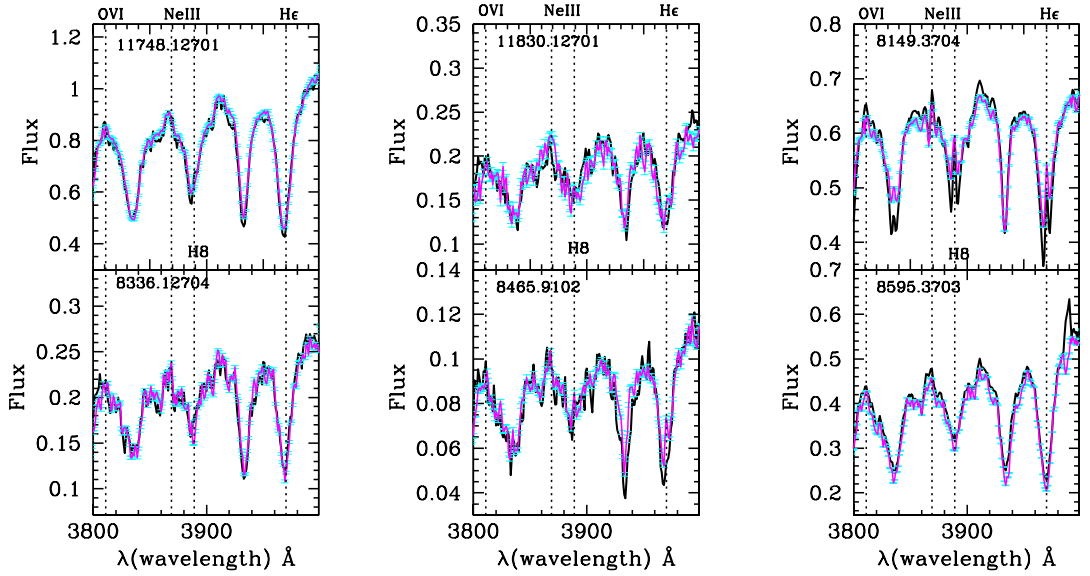

Figure 12. As in the previous figure, except comparing stacked spectra from Hα excess spaxels in the 6 galaxies with no WR feature detections with stacked spectra from normal starburst spaxels. Results are shown for the 8 galaxies with WR feature detections. Errorbars on the Hα excess spectra are plotted in cyan.

at wavelengths close to 6374 Å. The stacked spectra from the Hα excess spaxels are plotted in red and the stacked spectra from the normal starburst spaxels are plotted in black. We note that we also searched the spectra of the 6 galaxies with no Wolf–Rayet detections for emission lines in the neighbourhood of 6374 Å emission and did not find any clear detections.

One possible contaminant is [O I]λ6363, which is expected to be about three times weaker than [O I]λ6300 for starburst galaxies

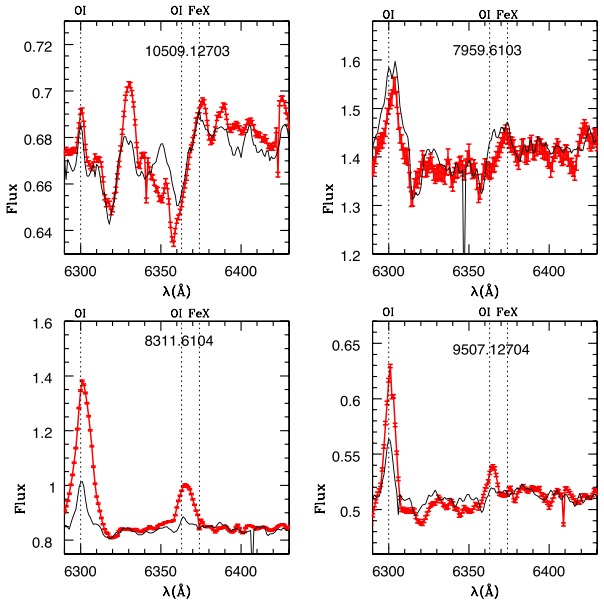

Figure 13. The region of the spectrum containing the [Fe X] coronal line. This line is often used as an AGN indicator, though it can also be produced in SNII shocks. Four galaxies from the sample with WR detections have [Fe X] detections and spectra in the regions of this line are plotted in the figure. The stacked spectrum from the H α excess spaxels is plotted in red and the stacked spectrum from the normal starburst spaxels is plotted in black. The sample without WR detections was checked and no [Fe X] line detections were found. The location of the two [O I] lines at 6300 and 6363 Å are also indicated on each panel.

(Heckman, private communication). In order to distinguish between [O I] and [Fe X], we plot the spectra over the wavelength range that includes [O I]λ6300. The emission features in the two galaxies 8311.6104 and 9507.12704 are quite consistent with [O I] emission.

The galaxy 10509.12703 exhibits a weak [Fe X]λ6374 line centred at 6374 Å rather than 6363 Å as is the case in the galaxies in the two bottom panels. There is also a very strong absorption feature bluewards of the emission line that is seen in both the nuclear and in the outer regions of the galaxy. It is possible that the [Fe X]λ6374 emission line may trace shocked outflowing gas in this system. The galaxy is not interacting and the ionized gas kinematics is dominated by rotation. We note that the [S III]λ9531 line is narrow and symmetric even in the H α excess regions in this object, so if there is an outflow, it is confined to the extremely highly excited gas.

The galaxy 7959.6103 exhibits weak but broad emission that spans the wavelength range between [O I]λ6363 and [Fe X]λ6374 emission. Interestingly, the emission line is narrower in the stacked spectrum covering the H α excess region (red spectrum) and it is also more clearly centred at 6374 Å. This galaxy is rather different from most of the others studied in this paper in that the H α excess spaxels are fewer in number and located entirely outside the central region of the galaxy. Their stacked spectrum exhibits a very strong broad He II λ4686 line excess, but there is no red bump or [Ne III]λ3869 emission line excess. Although the galaxy has a companion, the H α gas kinematics is regular and rotation dominated. The galaxy also has an earlier type morphology and all the emission lines are significantly weaker in this system than in most of the others. This suggests that this galaxy is a system where there are isolated pockets of Wolf–Rayet stars where gas has been locally compressed and shocked. As we will discuss in Section 8, if the starburst extends across a large region within the galaxy, it is likely that blue and red bump features will be seen simultaneously. If the starburst is confined to a very small region, this may not be the case because the blue and red bump features do not peak contemporaneously.

We note that the radio emission in the two objects with tentative [Fe X] line detections is weak (see Fig. 1) and they are also not the systems where the stacked H α excess spaxel spectra exhibit strong excess [Ne III]λ3869 emission, suggesting that these two lines may be excited by different physical mechanisms.

7 LOCAL ISM PROPERTIES

So far we have not found any clear explanation for why only some galaxies in the H α-selected sample show signatures of Wolf–Rayet stars. We have shown that Wolf–Rayet star regions are often associated with regions of the galaxy with very high-ionization line emission, but this is most likely a consequence of the the presence of these young massive stars (and possible associated accreting black holes), not an explanation of what causes them to form in the first place. We also showed that the ionized gas kinematics traced by the H α emission line within a radius R_{50} was indistinguishable in the two subsamples of galaxies with and without Wolf–Rayet detections (see Appendix Figs A3 and A4).

We now turn to an examination of colder neutral gas in these galaxies. We make use of the Na I $\lambda\lambda$5890, 5896 absorption line – the ionization potential of Na I is only 5.1 eV, so this absorption feature probes the neutral H I phase of the interstellar medium. It was first used as a probe of the neutral gas in a large sample of starburst galaxies by Heckman et al. (2000). The galaxies were selected on the basis of far-IR flux and very warm far-IR colour temperatures. The longslit spectra typically covered the inner few hundred to few thousand parsecs of each galaxy. In most galaxies, the absorption feature had a smaller velocity width than the stellar component in the same region, so dynamically cold interstellar gas was interpreted to be the main contribution to the observed NaD line. The NaD line was also found to be blueshifted by $\Delta v > 100\,\mathrm{km\,s^{-1}}$ relative to the galaxy systemic velocity in 12 out of the 18 cases, indicating that there were cold gas outflows in these galaxies. Finally, there was a strong correlation between the reddening of the stellar continuum and the depth of the absorption. Heckman et al. interpreted these observations in terms of an absorbing screen of gas and dust produced by gas outflowing along the minor axis of the the galaxy.

In this work, we compare the NaD absorption feature in the stacked spectrum covering the H α excess region of the starburst with that in the stacked spectrum covering the normal starburst regions. The comparison is thus of local ISM conditions in different regions of the same galaxy. In addition we compare results for the subsamples with and without Wolf–Rayet feature detections. Fig. 14 shows the stacked spectra in the region of the NaD doublet for the 8 galaxies with Wolf–Rayet feature detections. As can be seen, the doublets in the H α excess regions are almost always stronger than in the normal starburst regions. The only exception is galaxy 7959.6103.

We have measured the equivalent width of the NaD feature and the results are summarized in Fig. 15. In the top-left panel, the magenta triangles show the EQW measurements for the NaD absorption doublet in the stacked spectrum covering the H α excess spaxels for each of the 8 galaxies with WR feature detections. The black pinwheel symbols show the correspnding NaD EQW for the stacked spectrum of the normal starburst spaxels in each object. The difference between the magenta triangle and the black pinwheel at the same location of the x-axis is a measure of the change in NaD EQW between the two regions, which is typically around 2 Å in this subsample. In the top-right panel, we show the same plot for

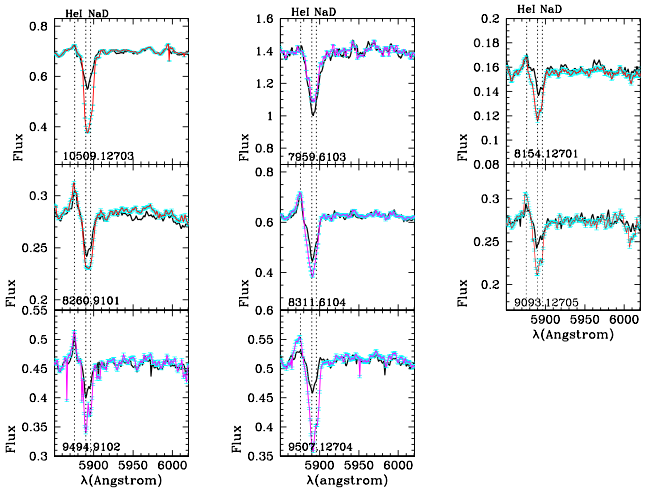

Figure 14. The region of the stacked spectra from Hα excess spaxels containing the NaD absorption line doublet (red or magenta lines) is compared to stacked spectra for spaxels with normal starburst values of the Hα equivalent width (black lines). Results are shown for the 8 galaxies with WR feature detections. Errorbars on the Hα excess spectra are plotted in cyan.

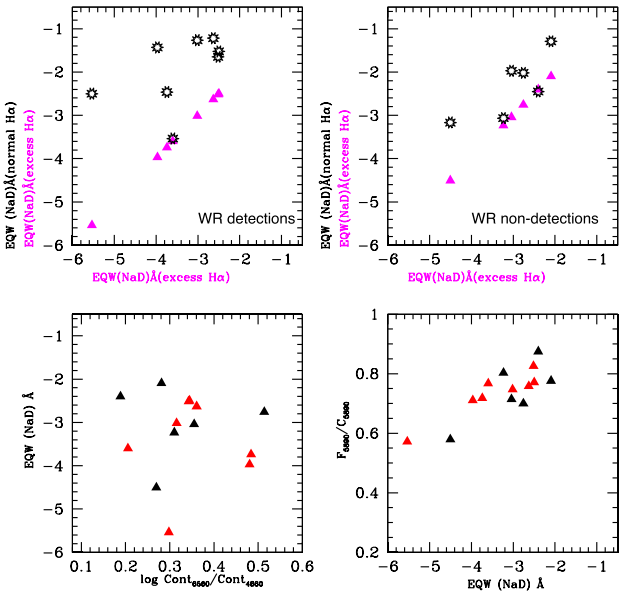

Figure 15. Top panel left: The magenta triangles show the EQW measurements for the NaD absorption doublet in the stacked spectrum for the Hα excess spaxels for each of the 8 galaxies with WR feature detections. The black symbols show the corresponding NaD EQW for the stacked spectrum of the normal starburst spaxels in each object. Top panel right: Same as the top-left panel, except for the 6 galaxies without WR detections. Bottom left: The NaD EQW in Hα excess regions is plotted against a measurement of the reddening in the stellar continuum. Red triangles are for the 8 galaxies with WR detections while black triangles for for the 6 galaxies without WR detections. Bottom right: the ratio of the NaD central flux decrement (defined as the flux at the centre of the line divided by the continuum flux) is plotted as a function of NaD equivalent width for the same two samples.

the subs-ample without Wolf–Rayet feature detections. The shift is considerably smaller, typically around 0.5 Å. Since the total range in NaD EQW is very similar in the two subsamples, we interpret these results as saying that greater cold gas *compression* may be important in explaining the presence of excess Wolf–Rayet stars.

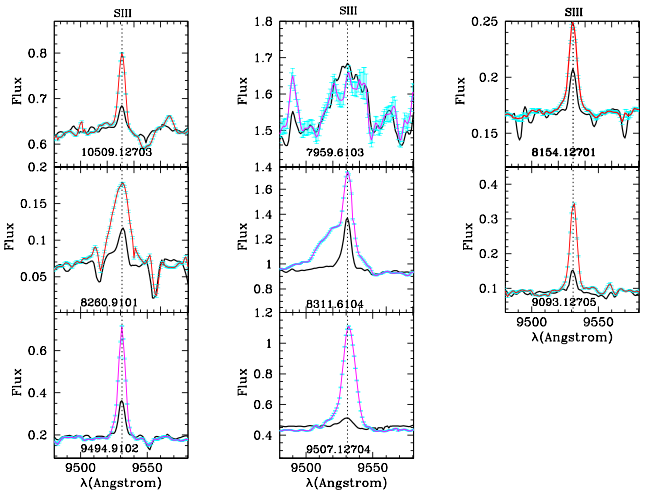

Figure 16. The region of the stacked spectra from Hα excess spaxels containing the [S III]λ9531 emission line (red or magenta lines) is compared to stacked spectra for spaxels with normal starburst values of the Hα equivalent width (black lines). Results are shown for the 8 galaxies with WR feature detections. Errorbars on the Hα excess spectra are plotted in cyan.

In the bottom-left panel, we examine whether there is a correlation between NaD EQW and dust in the Hα excess regions of starburst galaxies Red triangles are for the 8 galaxies with WR detections and black triangles are for the 6 galaxies without WR detections. No clear correlation is found in either sample. As discussed earlier, this is in strong contrast to the IR-selected starburst sample studied by Heckman et al. 2000. These results indicate that the dust and cold gas do not form a foreground screen in Hα-selected starbursts, but are more well mixed with the stars. We also note the the NaD doublets in the Hα excess galaxies do not exhbit significant blue-shifts (see Fig. 14) indicative of outflows.

In the bottom-right panel, the ratio of the NaD central flux decrement (defined as the flux at the centre of the line divided by the continuum flux) is plotted as a function of NaD equivalent width for the same two samples. Only a weak correlation is seen and the flux decrements do not extend to the very low values (∼0.1-0.2) found in the sample studied in the Heckman et al. (2000) paper, again indicating a deviation of ISM conditions in these galaxies from IR-selected starbursts.

To gain further insight, we examine local ISM conditions in the same way using the [S III]λ9531 emission line previously used for selecting regions likely to contain Wolf–Rayet stellar features. Fig. 16 shows the stacked spectra in the region of the line for the 8 galaxies with Wolf–Rayet feature detections. The line is always stronger in the Hα excess stack except, once again, for galaxy 7959.6193. The line also varies in width and exhibits a blue-side asymmetry in some cases.

Results on the properties of the [S III]λ9531 line are shown quantitatively in Fig. 17. In the top panel, the full width at half-maximum (FWHM) of the line is plotted against the line equivalent width. Results are only shown for the stacked spectra covering the Hα excess regions of the galaxies. Results for the subsample with detected Wolf–Rayet features are plotted as magenta triangles and results for the sample without Wolf–Rayet detections are plotted as black triangles. As can be seen, the FWHM for the galaxies in the sample without Wolf–Rayet detections is around 200 km s^{-1}. Half of the galaxies in the sample with Wolf–Rayet detections have larger FWHM line widths. The largest line widths are found for the lowest

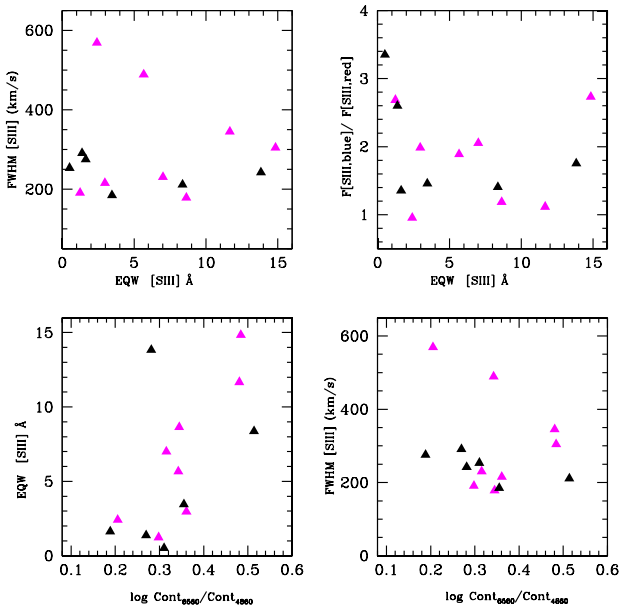

Figure 17. Top left: The FWHM line width of the [S III]λ9531 emission line is plotted against the line equivalent width in the stacked spectra for the H α excess spaxels. Magenta symbols show results for the eight galaxies with WR feature detections, while black symbols are for the 6 galaxies without WR detections. Top right: The line asymmetry index, defined as the total flux bluewards of line centre dived by the total flux redwards of line centre is plotted as a function of line equivalent width for the two samples. Bottom left: [S III] line equivalent width is plotted as function of the continuum reddening. Bottom right: the FWHM of the line is plotted as a function of the continuum reddening.

equivalent width systems. In the top-right panel, the ratio of the flux bluewards of line centre to the flux redwards of line centre is plotted as a function of line equivalent width. This ratio is greater than 1 for all the galaxies and reaches values of around 2 or greater for 5 out of 8 systems with Wolf–Rayet features and 2 out of 6 galaxies without WR features.[1]

In the bottom-left panel of Fig. 17, the [S III]λ9531 equivalent width is plotted as a function of the same continuum reddening parameter as in the bottom-left panel of Fig. 15. In this case, there is a clear correlation with continuum reddening. The H α excess galaxies tend to have higher [S III] equivalent widths and more reddening. In the bottom-right panel of Fig. 17, we plot the FWHM of the line as a function of continuum reddening. We find an anticorrelation in the sense that the less reddened systems have higher line widths. These results may indicate that the the dust is being expelled together with the ionized gas, and that the neutral gas remains locked in the interstellar medium within the disc.

In summary, we conclude that the H α excess regions of the galaxy are associated with higher neutral gas densities than normal starburst regions. If Wolf–Rayet stars are present, this difference is even larger. We interpret this as saying that Wolf–Rayet stars are produced when the ambient interstellar gas is compressed to unusually high densities. There is clear evidence of outflowing, dusty ionized gas associated with WR excess regions in the disc, but little evidence of outflowing neutral gas.

[1]Note, however, that the 2 galaxies without WR features with large values of this asymmetry parameter have small equivalent width, and the measurements may be more affected by continuum subtraction errors

8 MODELLING DISCUSSION: EFFECT OF IMF CHANGES PREDICTED BY HR-PYPOPSTAR

The measurement of equivalent widths of weak WR features is only possible if both the nebular emission and the contribution to the stellar continuum from older stars can be accurately modelled and subtracted. If the youngest stars reside in very dense, clumpy and dusty regions of the interstellar medium, the problem of modelling the stellar continuum becomes extremely challenging because continuum and line radiative transfer effects have to be considered not only through stellar atmospheres, but also through the surrounding dense molecular gas. As discussed in section 7, absorption lines from cold neutral gas are clearly present in all the galaxies in our sample and the strength of the absorption is higher for the galaxies with higher H α emission line equivalent widths.

In this paper, we do model and subtract the stellar continuum using libraries of template stars and then measure emission line strengths, as is usually done in galaxies that are forming stars at moderate rates. Instead, we look at the differential changes between regions where the extinction-corrected H α emission is exceptionally strong and regions where it has more normal values. The normal star-forming regions are usually situated at distances of 3–4 kpc from the centre of the galaxy. The crossing time across these regions can be estimated to be around 10^8 yr. One can use the Starburst99 code (Leitherer at al 1999) to show that a region that has formed stars at a constant rate for 10^8 yr with a Chabrier IMF will have an H α equivalent width of around 200. This value is in accord with the normal starburst region spaxels that are selected for stacking in our analysis. In contrast, the H α excess regions, which have H α equivalent widths in the range 800–2000, span regions of 1–1.5 kpc at most and the crossing time is closer to 3×10^7 yr.

We now use the population synthesis model HR-pyPopStar (Millán-Irigoyen et al. 2021) to generate predictions for the integrated spectra of star-forming regions. The HR-pyPopStar models provides a complete set (in ages) of high-resolution (HR) Spectral Energy Distributions of Single Stellar Populations. The model uses recent high-wavelength-resolution theoretical atmosphere libraries for main sequence (Coelho 2014), post-AGB/planetary nebulae (Rauch 2003), and OB and Wolf–Rayet stars (Hainich et al. 2019). The Spectral Energy Distributions are given for more than a hundred ages ranging from 0.1 Myr to 13.8 Gyr, at four different values of the metallicity ($Z = 0.004, 0.008, 0.019$, and 0.05). For the purposes of the analysis in this paper, it should be noted that the theoretical libraries of OB and Wolf–Rayet stars have additional free parameters relating to the adopted stellar wind models. For OB stars, the HR-pyPopStar models adopt moderate wind strengths, calculated with mass-loss rate, $\log \dot{M} = -7.0$. For WR stars, mass-loss rates are in the range $\log \dot{M}/(M_\odot/yr) = -4.3 - -6.1$.

We have combined the SSPs to predict the spectra of star-forming regions under the assumption that the star formation has been distributed uniformly over a time interval comparable to the crossing time across the regions. In detail, the normal star-forming regions are assumed to be represented by constant star formation for 10^8 years with a Chabrier IMF. We will call this the reference model henceforth. We then test two hypotheses for the spectra of the H α excess regions:

(i) Constant star formation for 3×10^7 yr with a Chabrier IMF.
(ii) Constant star formation for 3×10^7 yr with an IMF where the where the slope becomes flatter above $10\,M_\odot$.

For hypothesis (ii), we have generated spectra for the IMF explored in Kauffmann (2021) where the slope α in $dN/dM = m^{-\alpha}$ has a

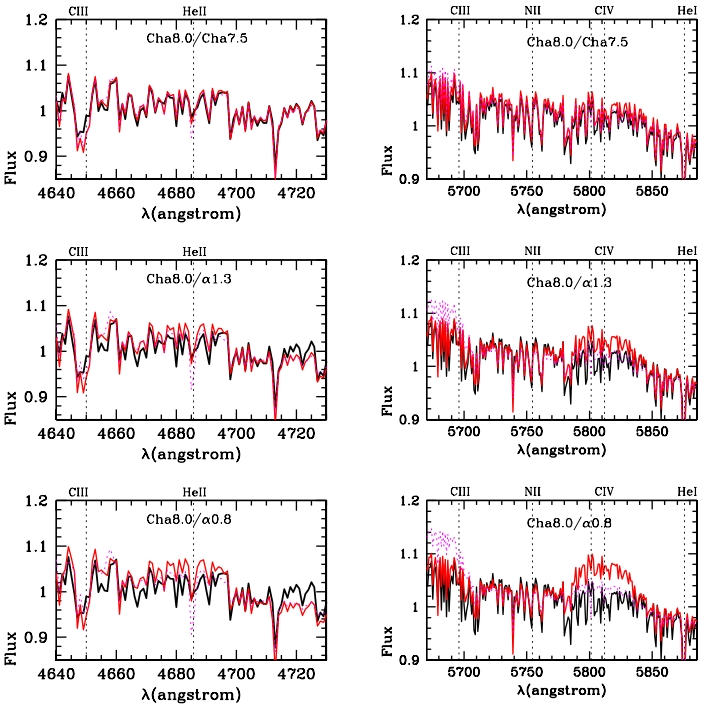

Figure 18. The reference model spectrum generated using HR-pyPopStar (Cha8.0)is compared with a variety of other model spectra plotted as coloured lines. In the top panels the coloured lines are for constant star formation rate lasting $10^{7.5}$ yr with a Chabrier IMF. Dotted magenta lines are for the dust-free case, while solid red lines include the effects of dust on the youngest stars as explained in the text. The middle and bottom panels are for models where the IMF has slope $\alpha = 1.3$ and $\alpha = 0.8$ above $10\,M_{\odot}$. All models for solar metallicity.

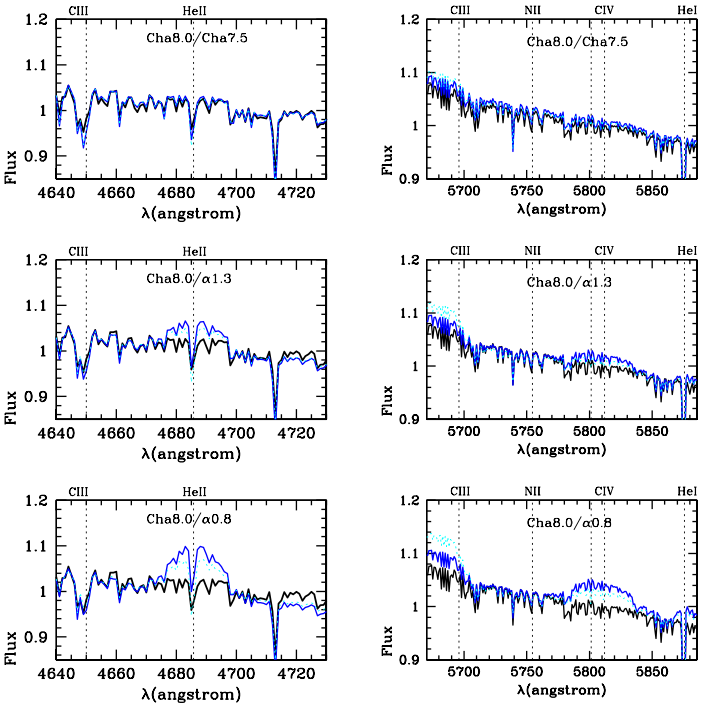

Figure 19. As in the previous figure, except at half solar metallicity.

value 0.8 above $10_{\odot}$, as well as a model with $\alpha = 1.3$. We note that the recent study of Hosek et al. (2019) found a slope $\alpha = 1.8$ for young stars in the galactic centre, so these IMF changes are fairly extreme. The models include the contribution from nebular continuum emission, but do not include nebular line emission. We use a very simplified approach to model the effect of differential extinction of the very youngest stars due to dust in stellar birth clouds by generating models where the very youngest stars with

ages less than 3×10^6 yr do not contribute to the optical spectrum. This time-scale is motivated by recent work by Kim et al. (2023) who used a combination of JWST and ALMA data for the nearby galaxy NGC 628 to measure the time-scale over which young stars remain heavily obscured while embedded in their parent molecular clouds. As we will show, obscuration of the youngest stars in the galaxies causes the Wolf–Rayet features to strengthen quite considerably in the predicted integrated spectra of model 2, because the phase of the evolution of massive stars associated with strong winds and mass-loss occurs at later ages ($10^7 - 3 \times 10^7$ yr after the birth of the star). Differences in continuum/line radiative transfer in the Hα excess and normal starburst ISM regions are neglected in this analysis.

In Fig. 18, we show how the predicted reference model spectra compare with models 1 and 2. Results in the figure are all calculated assuming solar metallicity. Fig. 19 shows the same for half solar metallicity models. The model spectra are all normalized to unity averaged over the wavelength range 4630–4750 Å in the left panels that show the blue bump features, and over the wavelength range 5670–5900 Å in the right panels that show the red bump features. The reference model is plotted in black in each panel. The spectra plotted as magenta/cyan dotted lines in Figs 18 and 19do not include any dust extinction. The spectra plotted as solid red/blue lines in the two figures assume that stars with ages less than 3×10^6 yr are completely obscured at optical wavelengths.

The top panels in Figs 18and 19 show almost no difference between the reference model spectrum and the spectrum of a region that has formed stars for a shorter time interval with the same IMF. This is true independent of whether or not dust extinction of the youngest stars is included. The middle and bottom panels show that significant (5–10 per cent) flux enhancements similar to those seen in the observations are only achieved for solar metallicty models where the IMF slope flattens at high masses and where the youngest stars are highly obscured. Differential extinction is less important for producing clear Wolf–Rayet bumps for the models with half solar metallicity. The blue bump around the He II λ4686 line is also stronger for the half solar model than for the solar model. Part of this difference may be caused by the fact that the continuum emission suffers less line-blanketing at lower metallicities, making the wind features easier to see in the spectra.

The Kauffmann (2021) IMF with $\alpha = 0.8$ above $10\,M_\odot$ combined with a constant star formation rate of 3×10^7 yr results in a predicted Hα equivalent width of 1500, which is nicely consistent with our adopted cut on EQW(Hα) used to define our Hα excess spaxels.

Some words of caution are now in order. An important issue that is not yet addressed is the fact that the Hα excess spaxels were not selected purely on the basis of Hα equivalent width, but in a two-dimensional space of EQW(Hα) and ionization parameter. Binary star systems are known to produce harder ionizing spectra and an alternative explanation for the observed spectral differences presented in this paper could be a larger fraction of interacting massive stars in the central dense ISM regions of our galaxies rather than an excess population of stars formed at higher masses. More detailed modelling comparing the photo-ionizing effects of interacting binaries with that of massive O stars, is required before further progress can be made (see for example Götberg et al. 2018).

We also note that the width of the red bump feature predicted by the models is comparable to the width of the excess emission in the observed spectra, but the same is not true for the blue bump emission, which is considerably narrower in the data than in the models. Assigning a fixed set of wind parameters to all Wolf–Rayet stars in the input stellar library is no doubt a serious oversimplification. Some of the WR lines such as CIIIλ5696 are very sensitive to the wind density. Finally, we note that the HR-pyPopStar models employ Padova isochrones (Bressan et al. 1993; Fagotto, et al. 1994; Girardi et al. 1996), which do not include the effects of stellar rotation on the evolution of stars – the lifetimes of massive stars are longer in these models and this will affect the predicted spectra. More detailed examination of these issues is deferred to future work.

9 SUMMARY AND FINAL DISCUSSION

We have extracted a sample of 17 nearby face-on galaxies from the final data release of the SDSS-IV MaNGA surveys where there are 100 or more spaxel resolution elements within the half-light radius and more than a dozen within $0.15R_{50}$. The galaxies are selected by applying the condition that the average Hα equivalent width (corrected for dust extinction) is 700 or more in at least one radial bin of width $0.1R_{50}$. A value of 700 is chosen because it cannot be explained by a starburst of any age if the stellar IMF has a Salpeter slope at the high-mass end. Spaxels with EQW(Hα) $>$ 700 define so-called Hα excess regions within the galaxies. Spaxels with EQW(Hα) $\sim$100 define normal starburst regions.

The goal of our study is to ascertain whether the Hα excess regions have an excess population of massive OB and Wolf–Rayet stars, to study the interstellar medium conditions in these areas of the galaxy, and to investigate whether there is evidence for accreting black holes in addition to stellar sources of ionization. We now summarize our main findings, dividing the discussion into three topics.

Wolf–Rayet star features:

(i) Selecting spaxels for stacking in the two-dimensional plane of Hα equivalent width and an emission line ratio that is insensitive to dust, is more effective at revealing Wolf–Rayet features that selecting on Hα alone. We have tested two diagnostics of ionization parameter: [O III]/Hβ and [S III]/[S II] and find that the second is more predictive in half of the galaxies.

(ii) 8 out of the 17 galaxies have detections of excess WR features in a stacked spectrum. Detections are not defined at a threshold equivalent width of a particular line, but by looking whether there is excess emission centred at either 4686 Å (the expected centroid of He II) or 5801 Å (the expected centroid of C IV) with respect to a 'control' stacked spectrum of spaxels from normal starburst regions of the same galaxy.

(iii) 6 out of the 8 galaxies with excess WR features have excesses both at 4686 and 5801 Å, that is, there is evidence for the presence of both WN and WC stars.

(iv) The regions of the galaxies with Wolf–Rayet features range in size from 300 pc to 1.5 kpc in diameter.

(v) They are usually located at or near the centre of the galaxy, but the WR region is often covers a elongated, cone-like region that is asymmetrically distributed with respect to the centre of the galaxy defined in optical broad-band emission.

Associated high-ionization emission line regions:

(i) *Only* the Hα excess spaxel regions where Wolf–Rayet features are detected exhibit strong high ionization lines. Excess [Ne III] is detected in 4 out of 8 of the WR regions and there are tentative [Fe X] detections in 2 galaxies.

Local interstellar medium conditions:

(i) We use the Na I $\lambda\lambda$5890, 5896 absorption line doublet as a probe of the cool neutral H I phase of the interstellar medium. The Hα excess regions are almost always associated with higher

equivalent width Na I absorption lines than the normal starburst regions. Significant velocity offsets of these features are not observed.

(ii) We use the difference in EQW Na I between the H α excess regions and the normal starburst regions as a probe of the cool gas compression in these regions. We find a larger gas compression factor in the regions where Wolf–Rayet features are also detected.

(iii) The FWHM and the centroid shift of the [S III]λ9531 emission line is used to probe physical conditions in the ionized gas. FWHM line widths greater than $\sim$ 200 km s^{-1} are only observed for the regions containing Wolf–Rayet stars. The [S III] line is always blue-shifted, indicating that the gas is outflowing. The [SIII] equivalent width correlated with the continuum reddening suggesting that the ionized, outflowing gas is carrying dust with it.

There are two main future challenges: (i) to constrain the nature of the young stellar populations in the central regions of the galaxies and (ii) to ascertain whether the high-ionization emission lines originate from matter accreting onto black holes, from radio-emitting jets or from from shocks produced by outflows from the central starbursts.

Further progress on (i) will require joint modelling of emission lines in HII regions and Wolf–Rayet star features. Götberg et al. (2019) investigate the impact of stars stripped in binaries on the integrated spectra of stellar populations, focusing specifically on the emission rates of H I-, He I-, and He II- ionizing photons assuming single-age bursts and continuous rates of star formation. They compare their results to results from the STARBURST99 models which do not include binaries, as well as the BPASS models (Stanway & Eldridge 2018), another population synthesis code that does include binaries.

The main result (see the right panel of Fig. 4 in the paper) is that in a single-age starburst, stripped stars dominate the H I and He I/He II ionizing budget at all ages greater than 15–20 Myr. In a system with continuous star formation, which we have argued is appropriate for the galaxies studied in this paper, stripped stars contribute less than 10 per cent of the H I-ionizing budget and less than half the He I-ionizing budget at all ages when compared to STARBURST99 models. In continuous models, stripped stars dominate the He II ionizing budget at ages greater than 10 Myr, similar to the single-age burst case. These results suggest that if the AGN and starburst contributions to the ionizing spectrum can be appropriately disentangled and the effects of dust properly accounted for, the combination of emission line and Wolf–Rayet star diagnostics in the integrated spectra of galaxies should be highly constraining.

Near-infrared IFU spectroscopy is very likely needed to provide a check on the results. The near-IR spectrum of the Circinius galaxy (Maiolino et al. 1997) reveals clear He I and Br γ emission, and a weak He II line detection in the wavelength range between 2.05 and 2.25 μm, where dust extinction effects are much less severe. Within the central 12 pc the starburst age is estimated to be about 7×10^7 yr, somewhat beyond the peak of the Wolf–Rayet phase, so it is likely that these features would be stronger in some of our more extreme systems such as 8311.6104.

Future progress on (2) relies on high-resolution imaging. The advent of a new era in large telescopes in space and advanced interferometric instrumentation on the ground will no doubt prove very interesting in the coming years.

ACKNOWLEDGEMENTS

We thank Tim Heckman for helpful comments that helped improve the analysis.

Funding for the SDSS-IV has been provided by the Alfred P. Sloan Foundation, the U.S. Department of Energy Office of Science, and the participating institutions.

SDSS-IV acknowledges support and resources from the Centre for High Performance Computing at the University of Utah. The SDSS website is www.sdss4.org.

SDSS-IV is managed by the Astrophysical Research Consortium for the Participating Institutions of the SDSS Collaboration including the Brazilian Participation Group, the Carnegie Institution for Science, Carnegie Mellon University, Centre for Astrophysics | Harvard & Smithsonian, the Chilean Participation Group, the French Participation Group, Instituto de Astrofísica de Canarias, The Johns Hopkins University, Kavli Institute for the Physics and Mathematics of the Universe (IPMU) / University of Tokyo, the Korean Participation Group, Lawrence Berkeley National Laboratory, Leibniz Institut für Astrophysik Potsdam (AIP), Max-Planck-Institut für Astronomie (MPIA Heidelberg), Max-Planck-Institut für Astrophysik (MPA Garching), Max-Planck-Institut für Extraterrestrische Physik (MPE), National Astronomical Observatories of China, New Mexico State University, New York University, University of Notre Dame, Observatário Nacional / MCTI, The Ohio State University, Pennsylvania State University, Shanghai Astronomical Observatory, United Kingdom Participation Group, Universidad Nacional Autónoma de México, University of Arizona, University of Colorado Boulder, University of Oxford, University of Portsmouth, University of Utah, University of Virginia, University of Washington, University of Wisconsin, Vanderbilt University, and Yale University.

10 DATA AVAILABILITY

The data underlying this study are publicly available at https://www.sdss4.org/dr17/manga/. Additional data products generated for the study, such as the stacked spectra, will be made available upon reasonable request to the corresponding author.

REFERENCES

Abdurro'uf et al., 2022, ApJS, 259, 35
Aguado D. S. et al., 2019, ApJS, 240, 23
Antonucci R., 1993, ARA&A, 31, 473
Baldwin J. A., Phillips M. M., Terlevich R., 1981, PASP, 93, 5
Blanton M. R., Kazin E., Muna D., Weaver B. A., Price-Whelan A., 2011, AJ, 142, 31
Bressan A., Fagotto F., Bertelli G., Chiosi C., 1993, A&AS, 100, 647
Brinchmann J., Kunth D., Durret F., 2008, A&A, 485, 657
Brown A., Nayyeri H., Cooray A., Ma J., Hickox R. C., Azadi M., 2019, ApJ, 871, L87
Bundy K. et al., 2015, ApJ, 798, L7
Chabrier G., 2003, PASP, 115, 763
Cid Fernandes R., Heckman T., Schmitt H., González Delgado R. M., Storchi-Bergmann T., 2001, ApJ, 558, L81
Coelho P. R. T., 2014, MNRAS, 440, 1027
Conti P. S., 1991, ApJ, 377, L115
Drissen L., Moffat A. F. J., Shara M. M., 1990, ApJ, 364, L496
Fagotto F., Bressan A., Bertelli G., Chiosi C., 1994, A&AS, 105, 29
Ferland G. J. et al., 2017, RMxAA, 53, 385
Ferland G. J., Korista K. T., Verner D. A., Ferguson J. W., Kingdon J. B., Verner E. M., 1998, PASP, 110, 761
Girardi L., Bressan A., Chiosi C., Bertelli G., Nasi E., 1996, A&AS, 117, 113
González Delgado R. M. et al., 1998, ApJ, 495, L698

Götberg Y., de Mink S. E., Groh J. H., Kupfer T., Crowther P. A., Zapartas E., Renzo M., 2018, A&A, 615, 78
Götberg Y., de Mink S. E., Groh J. H., Leitherer C., Norman C., 2019, A&A, 629, 134
Guo K. et al., 2019, ApJ, 870, L19
Guseva N. G., Izotov Y. I., Thuan T. X., 2000, ApJ, 531, L776
Hainich R. et al., 2019, A&A, 621, 85
Häring N., Rix H.-W., 2004, ApJL, 604, L89
Heckman T. M. et al., 1997, ApJ, 482, L114
Heckman T. M., Kauffmann G., Brinchmann J., Charlot S., Tremonti C., White S. D. M., 2004, ApJ, 613, L109
Heckman T. M., Lehnert M. D., Strickland D. K., Armus L., 2000, ApJS, 129, 493
Ho L. C., Filippenko A. V., Sargent W. L. W., 1997, ApJS, 112, 315
Hosek M. W. et al., 2019, ApJ, 870, L44
Jin G. et al., 2021, ApJ, 923, L6
Kauffmann G., 2021, MNRAS, 506, 727
Kauffmann G., Heckman T. M., 2009, MNRAS, 397, 135
Kauffmann G. et al., 2003, MNRAS, 346, 1055
Kauffmann G., Maraston C., Comparat J., Crowther P., 2022, MNRAS, 513, 1063
Kewley L. J., Groves B., Kauffmann G., Heckman T., 2006, MNRAS, 372, 961
Kim J. et al., 2023, ApJL, 944, L20
Kimbro E., Reines A. E., Molina M., Deller A. T., Stern D., 2021, ApJ, 912, L89
Kocevski D. D. et al., 2012, ApJ, 744, L148
Korista K. T., Ferland G. J., 1989, ApJ, 343, L678
Kroupa P., 2001, MNRAS, 322, 231
Lammers C., Iyer K. G., Ibarra-Medel H., Pacifici C., Sánchez S. F., Tacchella S., Woo J., 2023, ApJ, 953, 26
Law D. R. et al., 2016, AJ, 152, 83
Law D. R. et al., 2021, AJ, 161, 52
Leitherer C. et al., 1999, ApJS, 123, 3
Li C., Kauffmann G., Heckman T. M., White S. D. M., Jing Y. P., 2008, MNRAS, 385, 1915
Liang F.-H. et al., 2020, ApJ, 896, L121
Licquia T. C., Newman J. A., 2015, ApJ, 806, L96
Maiolino R., Thatte N., Kroker H., Gallimore J. F., Genzel R., 1997, ASPC, 113, 351
Marconi A., Hunt L. K., 2003, ApJL, 589, L21
Mendez A. J. et al., 2013, ApJ, 770, L40
Millán-Irigoyen I., Mollá M., Cerviño M., Ascasibar Y., García-Vargas M. L., Coelho P. R. T., 2021, MNRAS, 506, 4781
Miralles-Caballero D. et al., 2016, A&A, 592, 105
Molina M., Reines A. E., Latimer L. J., Baldassare V., Salehirad S., 2021, ApJ, 922, L155
Negus J. et al., 2023, ApJ, 945, L127
Oliva E., Salvati M., Moorwood A. F. M., Marconi A., 1994, A&A, 288, 457
Penston M. V., Fosbury R. A. E., Boksenberg A., Ward M. J., Wilson A. S., 1984, MNRAS, 208, 347
Pérez-Montero E., Hägele G. F., Contini T., Díaz Á.I., 2007, MNRAS, 381, 125
Pier E. A., Voit G. M., 1995, ApJ, 450, L628
Prieto M. A., Viegas S. M., 2000, ApJ, 532, L238
Rauch T., 2003, A&A, 403, 709
Reichard T. A., Heckman T. M., Rudnick G., Brinchmann J., Kauffmann G., Wild V., 2009, ApJ, 691, L1005
Rola C. S., Terlevich E., Terlevich R. J., 1997, MNRAS, 289, 419
Sánchez S. F. et al., 2012, A&A, 538, 8
Sanders D. B., Soifer B. T., Elias J. H., Madore B. F., Matthews K., Neugebauer G., Scoville N. Z., 1988, ApJ, 325, L74
Sanders R. L. et al., 2020, ApJL, 888, L11
Sargent W. L. W., Filippenko A. V., 1991, AJ, 102, 107
Schaerer D., Contini T., Pindao M., 1999, A&AS, 136, 35
Stanley F. et al., 2015, MNRAS, 453, 591
Stanway E. R., Eldridge J. J., 2018, MNRAS, 479, 75
Stern D., 2015, ApJ, 807, L129
Terlevich R., Melnick J., 1985, MNRAS, 213, 841
Tozzi G. et al., 2023, MNRAS, 521, 1264
Westfall K. B. et al., 2019, AJ, 158, 231
Wilson A. S., Raymond J. C., 1999, ApJL, 513, L115
Yan R. et al., 2016, AJ, 152, 197
York D. G. et al., 2000, AJ, 120, 1579
Zhang W., Kong X., Li C., Zhou H.-Y., Cheng F.-Z., 2007, ApJ, 655, L851

APPENDIX A: ADDITIONAL MAPS OF PHYSICAL QUANTITIES

In Figs A1 and A2, we show maps of the Balmer absorption line feature H8. We select this high-order line because it is never contaminated by emission and easily measured in all the spectra. To zeroth order it provides a measure of the age of the underlying stellar population, with strong absorption indicating a young stellar population and weak emission an older stellar population. The strength of the Balmer absorption feature peaks in stars of spectral types A–F and is weaker in O and B stars, so that in the very youngest starbursts, Balmer absorption lines such as H8 may also be weak. As can be seen in the two figures, H8 is almost always strongest in the central regions of the galaxies in both the WR-detected and non-detected subsamples. There is no clear difference in H8 values between the two subsamples. This is expected, because the Wolf–Rayet phase is short lived – The WR phase occurs $\sim 10^7$ yr after the initial starburst, compared to 10^9 yr for the H8 absorption line to reach maximum strength.

Figs A3 and A4 show the ionized gas velocity maps for the galaxies in the two subsamples. The velocities are measured from the shift of the centroid of the Hα emission line with respect to the systemic velocity. Each colour indicates a interval of 50 km s^{-1} in velocity. If we define galaxies to have a significant velocity gradient if there is a clear gradient spanning 200 km s^{-1} in total (i.e. clear regions with 4 different colours in the plots), we see that 5 out of 8 galaxies have significant velocity gradients in the subsample with WR detections and 4 out of 6 in the subsample withour WR detections. One galaxy in the WR-detected subsample exhibits strongly red-shifted emission across the enire region within R_{50} and two galaxies exhibit very weak velocity gradients. In the subsample with no WR detection, one

galaxy has strong blue-shifted emission across most of the region within R_{50} and one galaxy has a very weak velocity gradient. In conclusion, there is no clear difference in the kinematics of the ionized gas in the two subsamples.

APPENDIX B: THE BLUE AND RED BUMP REGIONS OF THE SUBSAMPLE WITH NO WOLF–RAYET DETECTIONS

Figs B1 and B2 show stacked spectra in the blue and red bump wavelength regions for the subsample listed in Table 1 as having no excess WR feature detections. As in Figs 9and 10, the stacked spectra

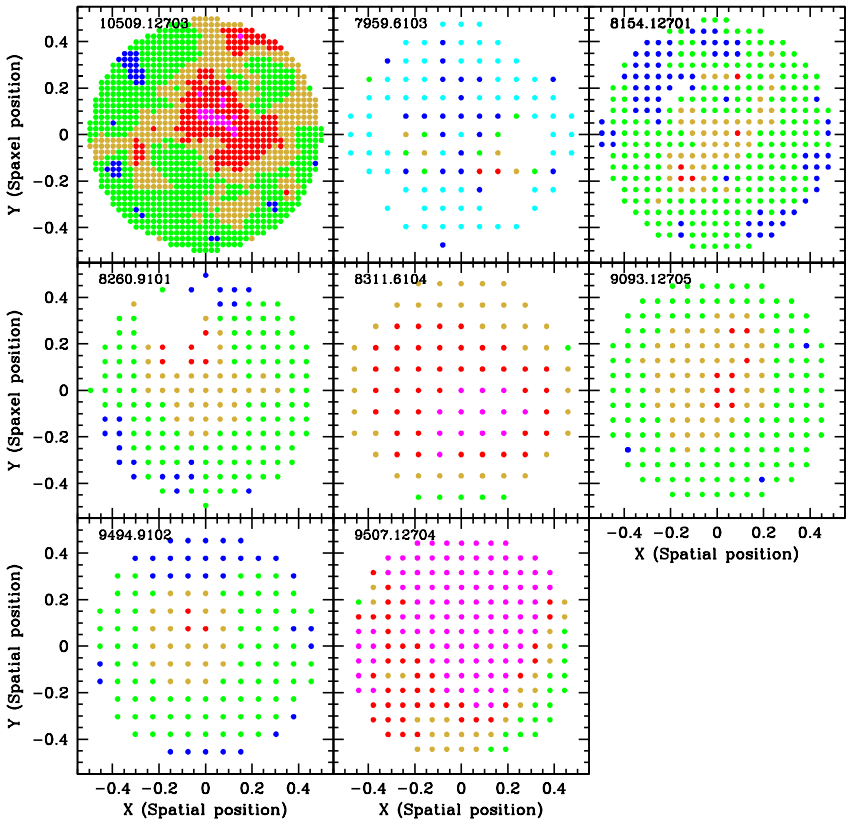

Figure A1. Two-dimensional maps of the Balmer absorption line index H8 for the 8 galaxies with Wolf–Rayet detections. The circular points indicate each spaxel measurement and are colour-coded as follows: magenta (H8 > 0.8), red (0.6< H8 < 0.8), dark gold (0.5< H8 < 0.6), green (0.4< H8 < 0.5), blue (0.3< H8 < 0.4), and cyan (0.2< H8 < 0.3).

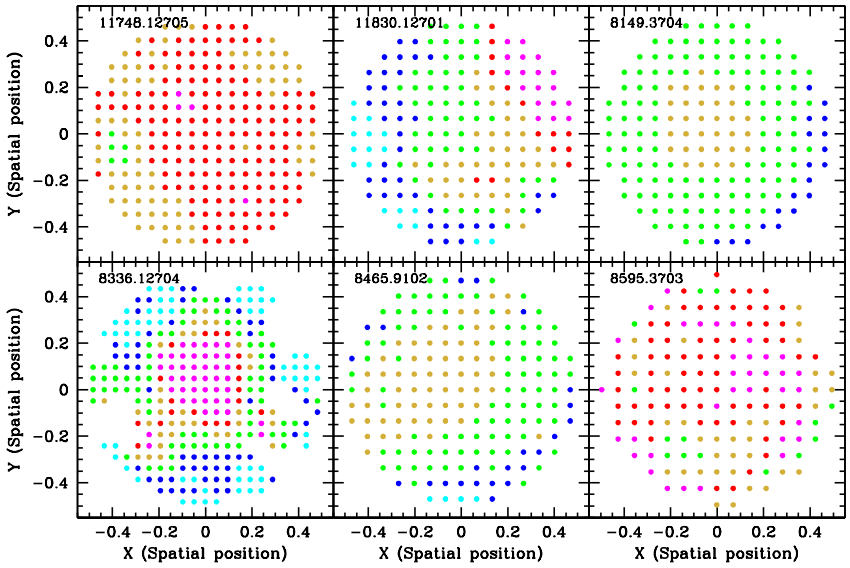

Figure A2. As in the previous figure, except for the 6 galaxies with no Wolf–Rayet detections.

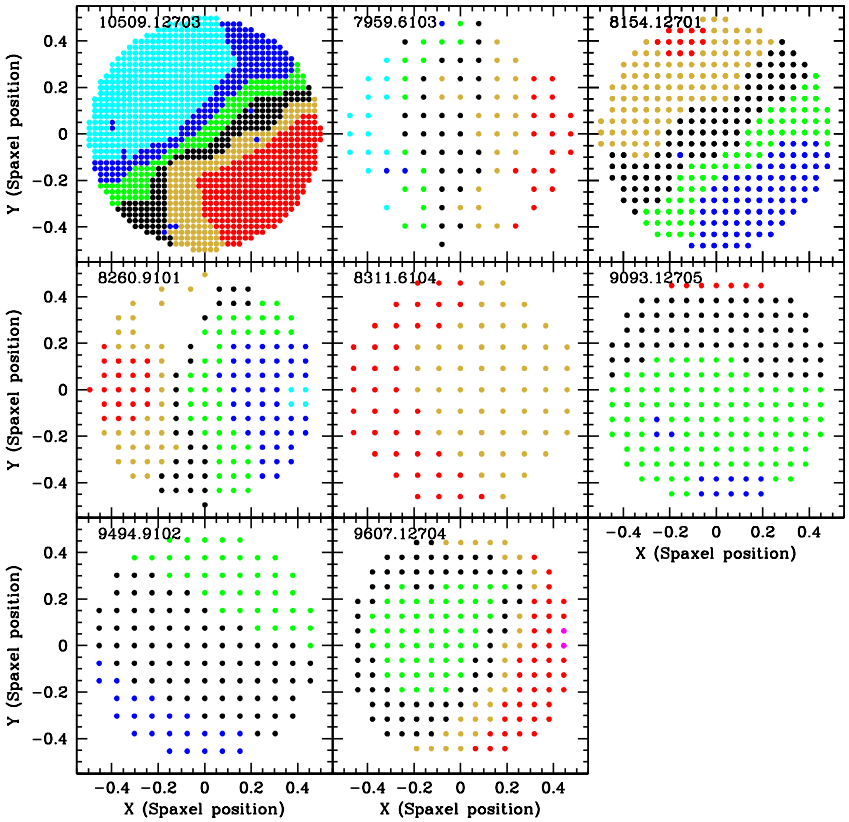

Figure A3. Two-dimensional maps of the velocity of the H α emission line for the 8 galaxies with Wolf–Rayet detections. The circular points indicate each spaxel measurement and are colour-coded as follows: black (0<V(H α) <50 km s^{-1}), green (0<V(H α) >−50 km s^{-1}), dark gold (50<V(H α) <100 km s^{-1}), blue (−50<V(H α) >−100 km s^{-1}), red (100<V(H α) <200 km s^{-1}), cyan (−100<V(H α) >−200 km s^{-1}), magenta (300 km s^{-1} <V(H α), and cyan bold ((−300 km s^{-1} >V(H α).

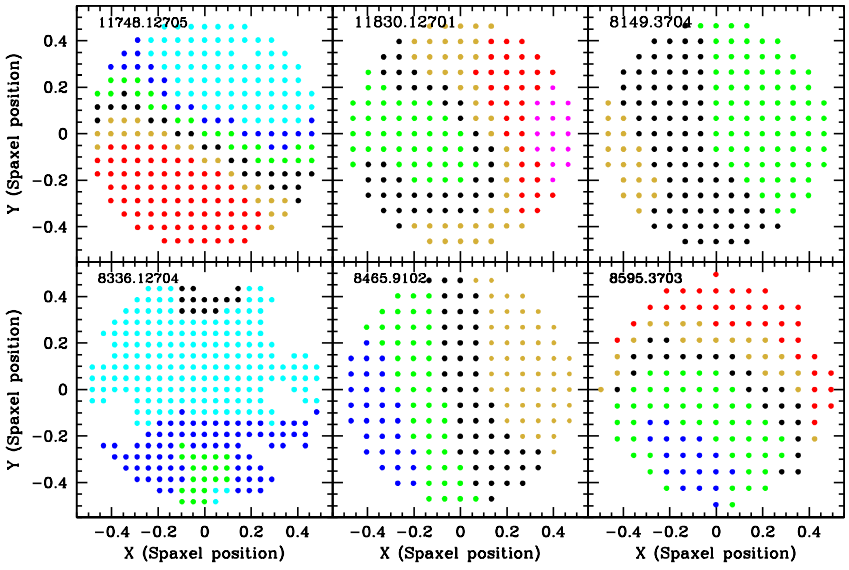

Figure A4. As in the previous figure, except for the 6 galaxies with no Wolf–Rayet detections.

of the regions with normal H α equivalent width values are plotted in back, while the stacked spectra of the H α excess regions are plotted in red. The 1σ error region on the H α excess stacked spectra are plotted in cyan. With the possible exception of object 8149.3704, no excess emission is seen close to the He II λ4686 or the C IV λ5801 lines.

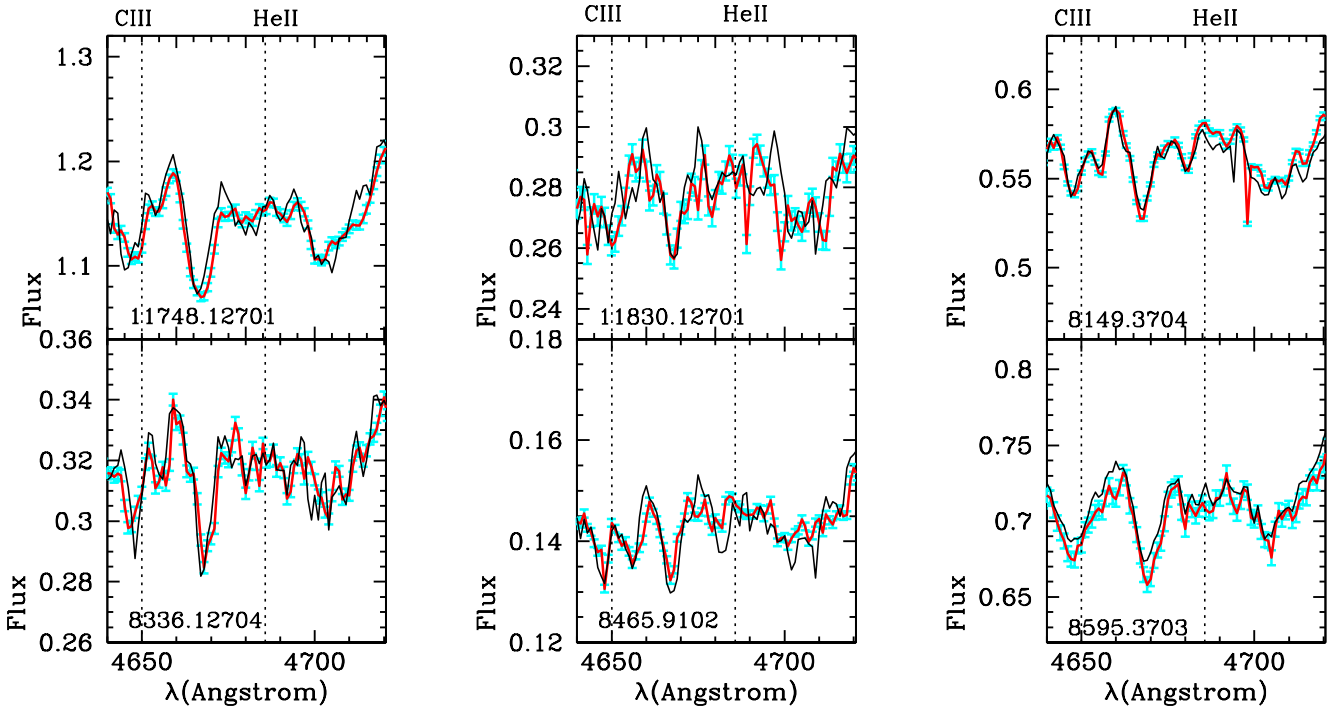

Figure B1. The 'blue bump' region of the stacked spectra is shown for the selected Hα excess spaxels (red or magenta lines) compared to the spaxels with normal starburst values of the Hα equivalent (black lines). Errorbars on the Hα excess spectra are plotted in cyan. All spectra are selected using a cut on log [O III]/Hβ (the attempt to select using sulphur line ratios did not result in better detections that shown.

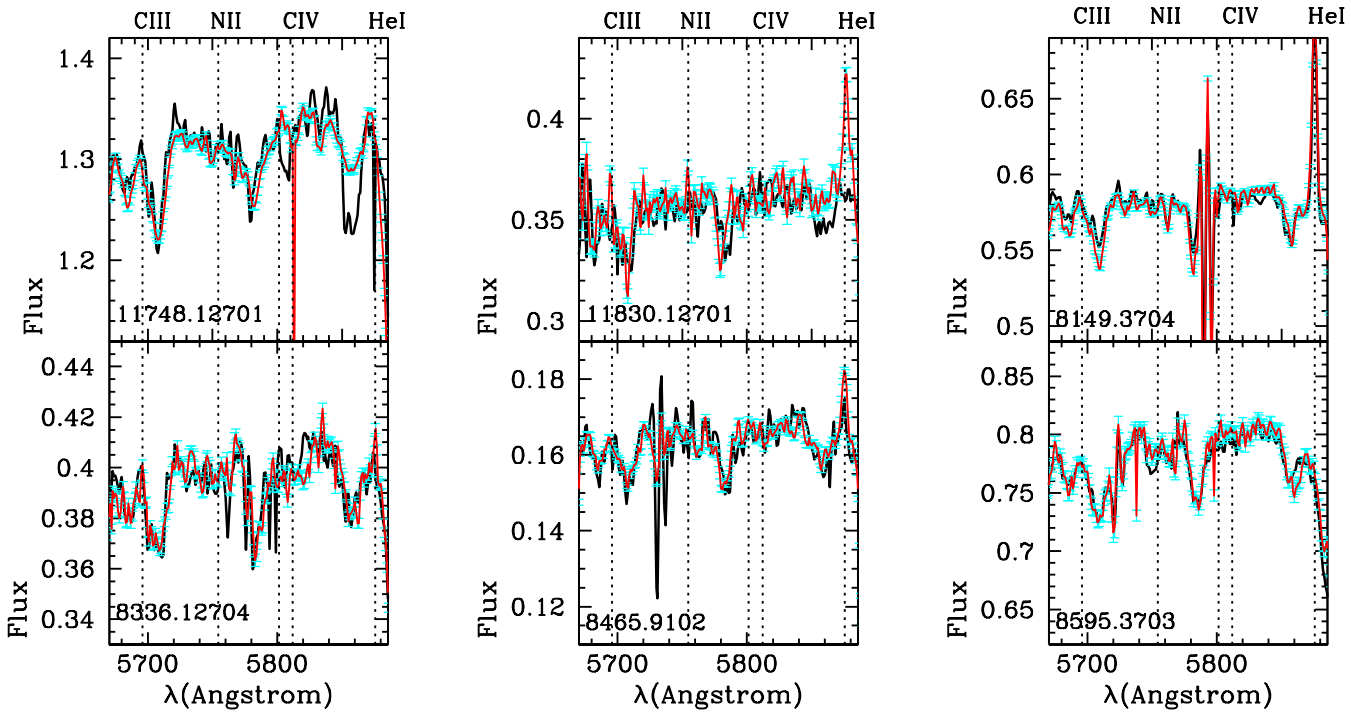

Figure B2. As in the previous figure, except for the 'red bump' region of the stacked spectra.

This paper has been typeset from a TEX/LATEX file prepared by the author.